

RESOLUTION OF FISSION AND FUSION TECHNOLOGY INTEGRATION ISSUES: AN UPGRADED DESIGN CONCEPT FOR THE SUBCRITICAL ADVANCED BURNER REACTOR

FISSION REACTORS

KEYWORDS: *subcritical reactor, fast burner reactor, transmutation reactor*

W. M. STACEY,* C. L. STEWART, J.-P. FLOYD, T. M. WILKS, A. P. MOORE, A. T. BOPP, M. D. HILL, S. TANDON, and A. S. ERICKSON

*Georgia Institute of Technology, Nuclear & Radiological Engineering Program
Atlanta, Georgia 30332-0745*

Received June 19, 2013

Accepted for Publication September 10, 2013

<http://dx.doi.org/10.13182/NT13-96>

The conceptual design of the subcritical advanced burner reactor (SABR), a 3000-MW(thermal) annular, modular sodium pool-type fast reactor, fueled by metallic transuranic (TRU) fuel processed from discharged light water reactor fuel and driven by a tokamak D-T fusion neutron source based on ITER physics and technology, has been substantially upgraded. Several issues related to the integration of fission and fusion technologies have been addressed, e.g., refueling a modular sodium pool reactor located within the magnetic coil configuration of a tokamak, achieving long-burn quasi-steady-state plasma operation, access for heating and current drive power transmission to a toroidal plasma surrounded by a

sodium pool fast reactor, suppression of magnetohydrodynamic effects in a liquid metal coolant flowing in a magnetic field, tritium self-sufficiency in a TRU transmutation reactor, shielding the superconducting magnets from fusion and fission neutrons, etc. A design concept for a SABR that could be deployed within 25 years, based on the IFR/PRISM metal-fuel, sodium pool fast reactor technology and on the ITER fusion physics and technology, is presented. This design concept can be used for realistic fuel cycle, dynamic safety, and other performance analyses of a SABR.

Note: Some figures in this paper may be in color only in the electronic version.

I. INTRODUCTION

The concept of combining fusion, which can produce copious neutrons, with assemblies of fissionable or fertile material, which can use those neutrons to produce copious amounts of energy via fission or to produce new fissionable material via neutron transmutation, has been around since the early days of nuclear power.¹⁻⁶ More recently, in the United States, the concept of using fusion neutrons to fission the actinides remaining in used nuclear fuel⁷⁻¹⁰ has attracted some attention, but

the neutron transmutation of fertile material into fissionable material also remains of interest^{11,12} for the longer term.

At Georgia Institute of Technology (Georgia Tech), we are pursuing the concept of combining the leading metal-fuel, sodium-cooled IFR/PRISM fast reactor technology¹³⁻¹⁶ with the leading tokamak fusion technology being incorporated in the ITER fusion experimental power reactor^{17,18} in the subcritical advanced burner reactor^{7,8} (SABR), which would utilize as fuel the processed transuranics (TRUs) remaining in used fuel removed from conventional nuclear power reactors. We believe that subcritical operation of a fast burner reactor would have certain advantages relative to critical

*E-mail: weston.stacey@nre.gatech.edu

operation, namely, that in a subcritical reactor (a) the much larger reactivity margin to prompt critical would allow the use of 100% TRU fuel (thus requiring fewer transmutation reactors) and (b) since the burnup reactivity decrement would be offset by increasing the fusion neutron source strength, the number of reprocessing steps could be minimized by leaving the fuel in the reactor until it reached the radiation damage limit (thus requiring fewer batches of fuel, less refueling downtime, and fewer high-level-radioactive-waste repositories).

An initial design concept for SABR was developed a few years ago,⁷ and initial dynamic safety,¹⁹ fuel cycle,^{20,21} and materials scenario²² studies of the SABR concept have been performed to examine (a) the peaking of power distributions, fuel composition evolution, and neutron damage with irradiation; (b) the dynamic response of the system to various reactivity insertions and coolant system malfunctions; and (c) the reduction achievable in decay heat and required high-level-waste-repository capacity for fuel discharged from conventional reactors by using it as fuel for subcritical fast burner reactors rather than directly burying it.

However, these studies have also identified a number of fission-fusion technology integration issues—refueling the fast reactor located within the tokamak magnet system, access for the plasma heating and current drive (H&CD) systems with an annular fission core outboard of the plasma, the magnetohydrodynamic (MHD) effects on the liquid metal sodium coolant flow in the tokamak magnetic field, the effect of the structure required within the tokamak magnet system on the neutron multiplication of the fast reactor and on the tritium self-sufficiency, etc.—that need to be defined in somewhat greater detail. The purpose of this paper is to describe the revised and more detailed SABR concept that has been developed to address these and other fission-fusion technology integration issues.

Follow-up research has been initiated to (a) repeat and extend the fuel cycle, dynamic safety, and decay heat/repository capacity studies for the revised SABR concept and (b) compare the overall transmutation systems that would be needed with critical and subcritical (SABR) fast burner reactors for closing the back end of the nuclear fuel cycle. This research will be published in separate papers over the next few years.

II. DESIGN OVERVIEW

II.A. Design Objectives

The purpose of SABRs is to fission the TRUs in both the legacy used fuel and in the used fuel that will be discharged from the existing and near-future fleet of conventional light water reactor (LWR) nuclear power reactors, thereby reducing by at least an order of magnitude the storage capacity requirements for long-term high-level-waste repositories, while also extracting the energy content in that used fuel. The dominant guiding principle of the

previous SABR design^{7,8} and of this design upgrade is the utilization of state-of-the-art fast reactor and tokamak fusion physics and technology that will [by ITER (Refs. 17 and 18) in the case of fusion] or could (by a demonstration fast reactor and fuel reprocessing/refabrication system in the case of fast reactors) be demonstrated on a reactor scale in the near term to make deployment of the first SABR feasible within 25 years. Retention of the inherent safety characteristics that have been demonstrated for sodium pool-type fast reactors with metal fuel and achievement of tritium self-sufficiency are two other primary design objectives. It is our intent that this SABR design upgrade be based on plasma stability, confinement, noninductive current drive, and other plasma parameters in the upper range of the established database and confront the main fission-fusion technology integration and radiation shielding issues to provide a realistic basis for future dynamic safety and fuel cycle performance analyses of the SABR concept. Based on (a) the EBR-II operating experience, the design of the IFR and PRISM reactor concepts, and the assumption that a prototype fast reactor and associated fuel reprocessing and refabrication facilities will be operated within the next 25 years and (b) the operation of ITER as a prototype fusion neutron source in the 2020s, we adopt 75% availability for a 40-year lifetime as a design objective for SABR for the purpose determining shielding requirements and materials radiation damage.

II.B. Configuration

The SABR is a metal-fuel, modular sodium pool-type, annular fast reactor located just outboard of the plasma and within the toroidal field (TF) magnet coils of a sodium-cooled tokamak neutron source, as depicted in Fig. 1. The total power output is 3000 MW(thermal), mostly from fission but including several hundred megawatts thermal from fusion and exoergic neutron reactions. Ten 300-MW(thermal) modular sodium pools, each containing 80 fuel assemblies and an intermediate heat exchanger (IHX), comprise the annular fast reactor core. The toroidal and poloidal ring coil magnet systems are identical to those in ITER (Refs. 17 and 18), and other fusion technology is adapted from ITER.

II.C. Major Parameters and Materials

Table I describes the major parameters and materials of the upgraded SABR design. A detailed discussion of the choice of these parameters and materials is provided in the following sections.

III. FAST BURNER REACTOR

III.A. Fuel Assembly

The SABR fuel is based on the 40Zr-10Am-10Np-40Pu TRU fuel being developed at Argonne National

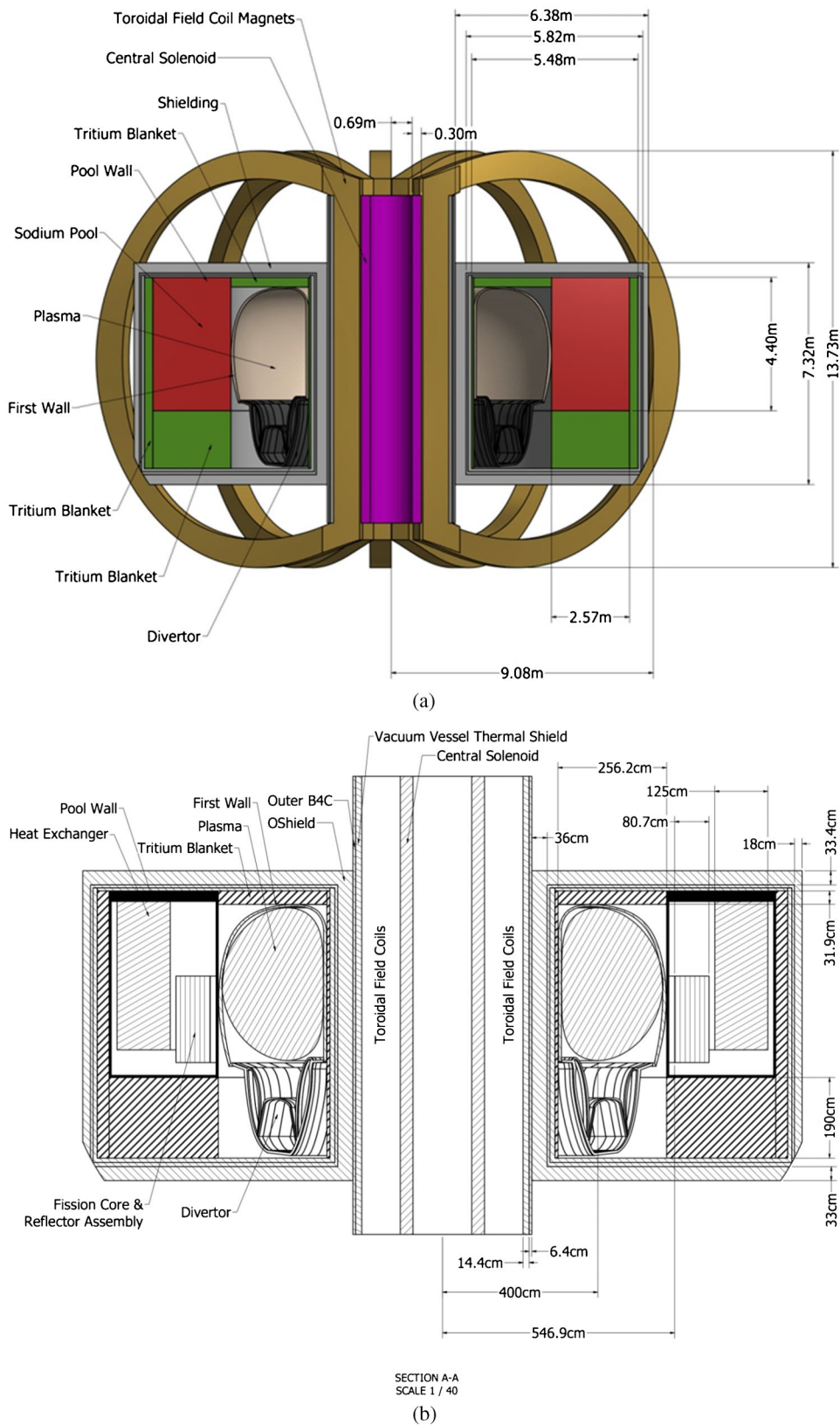


Fig. 1. (a) Perspective view of SABR configuration; (b) radial build of SABR configuration.

TABLE I

Major Parameters and Materials of the SABR Design

Fast reactor core TRU fuel composition BOL TRU mass BOL k_{eff} Specific power Fuel assembly Fuel pin Power density Linear fuel pin power Sodium coolant mass flow rate Coolant temperature (T_{incool} ; $T_{outcool}$) Fuel and clad temperature ($T_{maxfuel}$; $T_{maxclad}$) Clad and structure Electric insulator Fuel/clad/bond/insulator/duct/coolant/wire (vol %)	40Zr-10Am-10Np-40Pu 15 104 kg 0.973 198.6 W/g HM 800 469 per assembly, 375 200 total 256 kW/ ℓ 12.3 kW/m 16 690 kg/s 628 K; 769 K 1014 K; 814 K ODS MA957 SiC 22.3/17.6/7.4/6.5/9.3/35.3/1.5%
Tritium blanket Tritium breeder Sodium coolant mass flow rate Minimum and maximum blanket temperatures BOL TBR Startup T required	Li_4SiO_4 1 kg/s (3.8 m/s) 450°C, 574°C 1.12 0.7 kg
Reflector Materials—reflector assembly in-core (vol %) Materials—graphite reflectors (vol %)	ODS steel (58.1%), SiC (6.6%), Na (35.3%) Graphite (90%), Na (10%)
Shield Materials	Graphite, tungsten carbide, boron carbide, Na
Plasma Major radius Plasma radius Elongation Toroidal magnetic field (on-axis) Plasma current Inductive current startup Noninductive current drive Bootstrap current fraction H&CD power Confinement factor, H_{98} Normalized β_N Safety factor at 95% flux surface Maximum and BOL fusion power Maximum fusion neutron source strength Fusion gain ($Q_p = P_{fusion}/P_{exheat}$)	4.0 m 1.2 m 1.5 5.6 T 10 MA 6.0 MA 4.5 MA 0.55 110 MW (70 EC, 40 LH) 1.2 3.2% 3.0 500 MW and 233 MW 1.8×10^{20} n/s 4.6
Superconducting magnets Central solenoid Maximum field Flux core radius CS coil thickness Inductive flux TF coils Number Maximum field TF bore dimensions PF ring coils	Adapted from ITER CS system 13.5 T 0.69 m 0.3 m 59 V·s ITER TF system 10 (18 on ITER) 11.8 T 16.5 m (height) \times 9 m (width) ITER PF system

TABLE I
(Continued)

Plasma H&CD system	
EC current drive efficiency	0.025 A/W
EC power	70 MW
EC upper quadrant modules (7.25 MW each)	4 (30 MW total)
EC equatorial modules (20 MW each)	2 (40 MW total)
LH current drive efficiency	0.035 A/W
LH power	40 MW
LH number of modules (20 MW each)	2
Divertor	
Materials	Tungsten, CuCrZr, Na cooled
Power to divertor ^a	105 MW; 31.5 MW
Heat flux	1 to 8 MW/m ²
Sodium coolant mass flow rate	0.09 kg/s
First wall	
Materials	Be, CuCrZr, ODS steel
Thickness	8.1 cm (1 cm Be, 2.2 cm CuCrZr, 4.9 cm ODS steel)
14-MeV fusion neutron power flux (average)	1.7 MW/m ²
Fission + scattered fusion neutron power flux	0.6 MW/m ²
Surface heat flux ^a	0.44 MW/m ² ; 0.74 MW/m ²
Sodium coolant mass flow rate	0.057 kg/s
Sodium pool	
Number of modular pools	10
Mass of fuel per pool	1510.4 kg
Mass of Na per pool	22 067 kg
Power per pool	300 MW
Mass flow rate per pool	1669 kg/s
Number of pumps per pool	2
Pumping power per pool	20 MW

^aThe first number is for a 50/50 split between charged particles and radiation across the separatrix, and the second number is for a 15/85 split.

Laboratory (ANL) and is discussed in detail in Ref. 7. The SABR fuel assemblies are adapted from the S-PRISM assemblies.¹⁶ There is one significant modification made to the assembly to reduce the MHD pressure drop: a 3-mm-thick flow channel insert (FCI) made of SiC (Ref. 23) is placed within the duct to prevent current loops from completing through the duct wall. There is a small gap between the FCI and the duct to prevent stresses between the two different materials and which is filled with the sodium coolant; however, this coolant does not need to flow to remove heat from the core, as there is no fuel in this region. The FCI design is derived from those proposed for the ITER liquid metal coolant tritium breeding modules.²³ The dimensions of the assembly cross section are given in Table II. With the exception of the axial shielding in each pin, which has been reduced to 15 cm, and the fission gas plenum, which retains the plenum-to-fuel volume ratio of 2.5 from S-PRISM, the nonfuel axial partitions of the assemblies are retained from the S-PRISM designs. The location of control rods will be determined later when the fuel cycle and dynamic

TABLE II
Assembly Cross-Section Description

Pin diameter	0.539 cm
Pin pitch	0.6346 cm
Pin pitch/diameter	1.177
Fuel diameter	0.370 cm
Cladding thickness	0.0559 cm
Cladding material	ODS MA957
Bond material	Na
Fuel smear density	75%
Assembly pitch	16.142 cm
Duct outer across flats	15.710 cm
Duct thickness	0.394 cm
Gap between duct and FCI	0.200 cm
FCI outer across flats	14.522 cm
FCI thickness	0.300 cm

safety analyses are carried out. Table III shows the axial partition data for the fuel assemblies using the S-PRISM notation.¹⁶

TABLE III
Fuel Assembly Axial Parameters

Assembly Axial Partition	Height (cm)
Upper handling socket	30.480
Handling socket – duct overlap	0.686
Duct standoff	4.445
Pin upper end plug	2.540
Fission gas plenum	121.875
Core	65.0
Lower shielding and end plug	15.0
Pin-grid overlap	0.914
Pin support grid	5.182
Grid–nose piece overlap	1.727
Duct–nose piece overlap	3.048
Nose piece	33.020
Pin (total)	204.415
Duct (total)	215.135
Assembly (total)	274.901

Each assembly houses a hexagonal lattice of 469 fuel pins. These pins are taken from the ANL zero conversion ratio (CR = 0) core design carried out for the Advanced Fuel Cycle Initiative.¹⁵ The CR = 0 core had three pin designs with varying assembly fuel volume fractions to

flatten the radial power profile; SABR uses only the largest of these, because the external neutron source and high leakage factor reduce power peaking and therefore the need for power shaping. The outside of the cladding of each pin is coated in a thin layer of SiC for electrical insulation over which is a layer of oxide dispersion strengthened (ODS) steel to prevent insulation breakdown in the event of crack formation in the SiC (Ref. 24). These layers, which prevent current loops from completing through the fuel pins, are of the order of a few microns thick, and the outer metal layer is thin enough that it has sufficient resistance. Figure 2 shows the fuel assembly cross section, and Fig. 3 shows the dimensions of the fuel pins.

III.B. Sodium Pools

The fissionable material is contained in ten modular sodium pools, which form a fission annulus within the TF coils, as depicted looking down from above in Fig. 4. The pools are sized to be removable radially in and out between the TF coils in two locations (at pools 1 and 6) to facilitate refueling. The vertical separation of 4.4 m between the two most equatorial poloidal field (PF) coils sets the maximum height of each modular sodium pool. The minimum separation between TF coils is 4.4 m at the pool location.

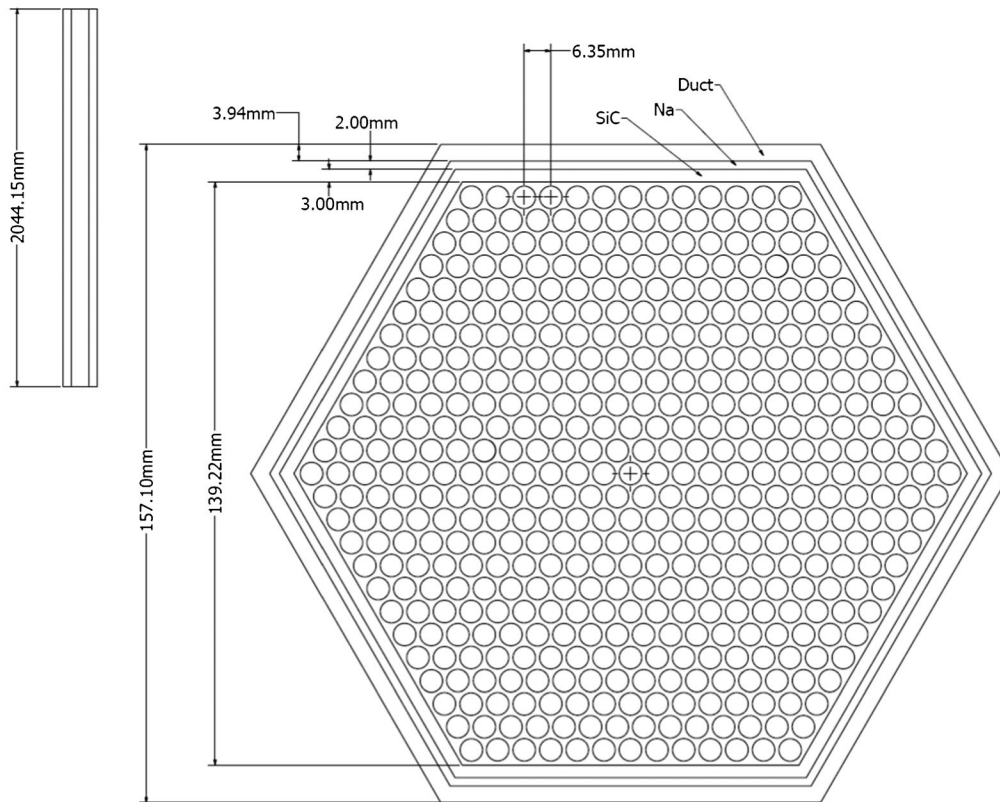


Fig. 2. SABR fuel assembly configuration.

Figures NOT TO SCALE

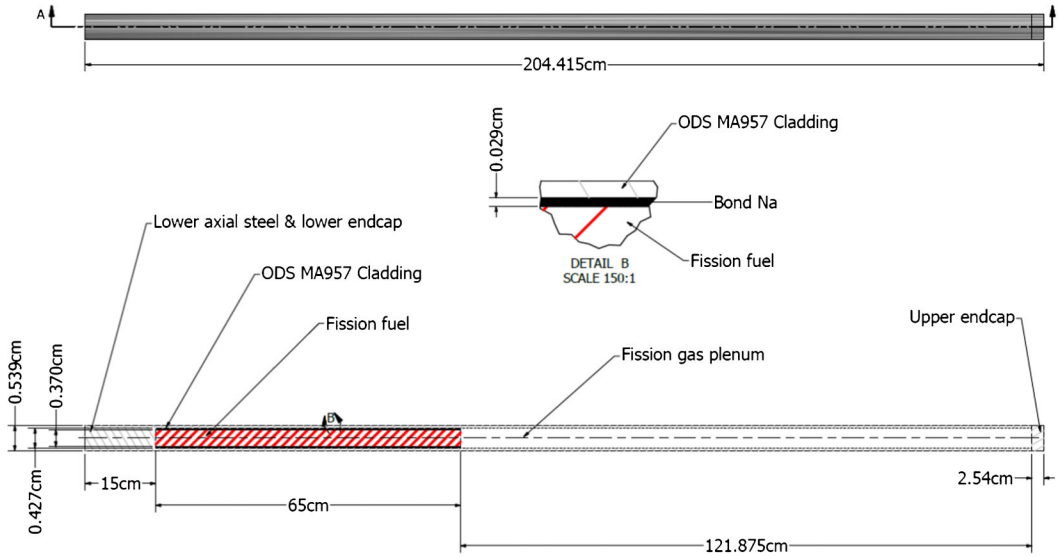


Fig. 3. SABR fuel pin configuration.

The ten pools occupy ~88% of the annulus, as shown in Fig. 4. The remainder of the annulus consists of two H&CD ports at locations 180 deg apart to bring power into the plasma. On either side of each of these H&CD ports are four small wedge-shaped tritium blankets (TB5 through TB8). The locations of the TF coils are indicated by the spokes extending radially outward in Fig. 4.

The sodium pool vessels, like the cladding, are made of ODS MA957 (Ref. 25) the inner surface of each vessel is coated with electrical insulator. A stress analysis was performed in Autodesk Inventor Professional 2013 to estimate the necessary thickness of the vessel walls. The pressure from the sodium and the weight of the fuel, reflector, and core grid plate provided the primary loading. Because the outside of the vessel is not exposed to air, the thermal gradient across the wall is very small, and thermal stresses are negligible.

According to the American Society of Mechanical Engineers (ASME) code, the allowable limits for nuclear pressure vessels can be expressed as

$$\sigma_p \leq S_{mt}(t)$$

and

$$\sigma_p + \sigma_{th} \leq \begin{cases} 1.5S_m(t) \\ K_t S_t(t) \end{cases},$$

where

$$S_{mt}(t) = \text{lower of } S_m(t) \text{ and } S_t(t)$$

S_m = lowest of one-third of the yield or ultimate tensile strength at room or operating temperature

$S_t(t)$ = lowest of the minimum stress necessary to cause 1% total strain in time t , two-thirds of the minimum stress to cause creep rupture in time t , or 80% of the minimum stress to cause the onset of tertiary creep in time t

σ_p = hoop stress in the vessel wall

σ_{th} = thermal stress in the vessel wall.

The quantity K_t is

$$K_t = 1 + \frac{1}{2} \left(1 - \frac{\sigma_p}{S_t} \right).$$

The yield and ultimate tensile strengths of ODS MA957 at 700°C are both 400 MPa (Ref. 26); at the operating temperature of 650°C, these strengths are higher. Creep rupture and strain data^{25,27} were estimated at a temperature of 650°C for a time of $t = 10$ years. From these, values of $S_m = 133$ MPa, $S_t = 150$ MPa were calculated.

For a vessel wall thickness of 1 cm, the maximum calculated stress was 100.5 MPa, which was sufficiently low to meet the ASME criteria. The pool's upper end cap, which supports the structure, is 25 cm thick. The vessel is shaped such that it follows the curvature around the plasma first wall as closely as possible to maximize the solid angle of the fission core with respect to the fusion neutron source. The vessel on which the stress analysis was performed has rounded corners and an elliptically

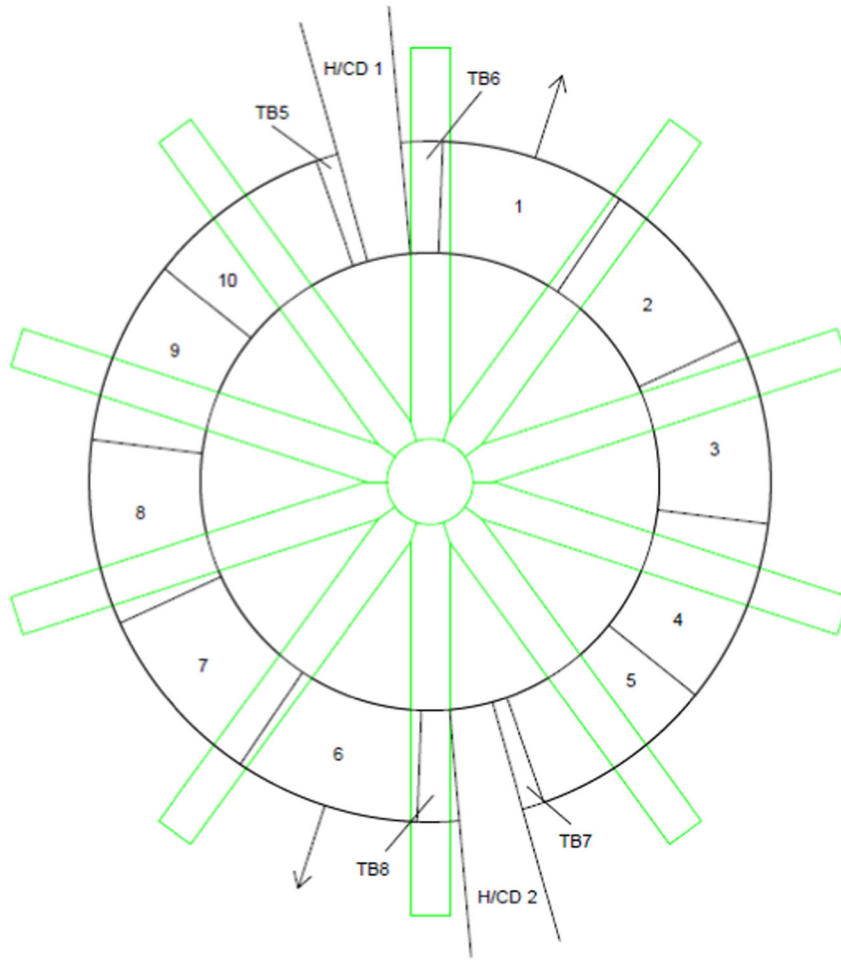


Fig. 4. Layout of the sodium pools, H&CD ports, and wedge-shaped tritium blankets (TB5 through TB8).

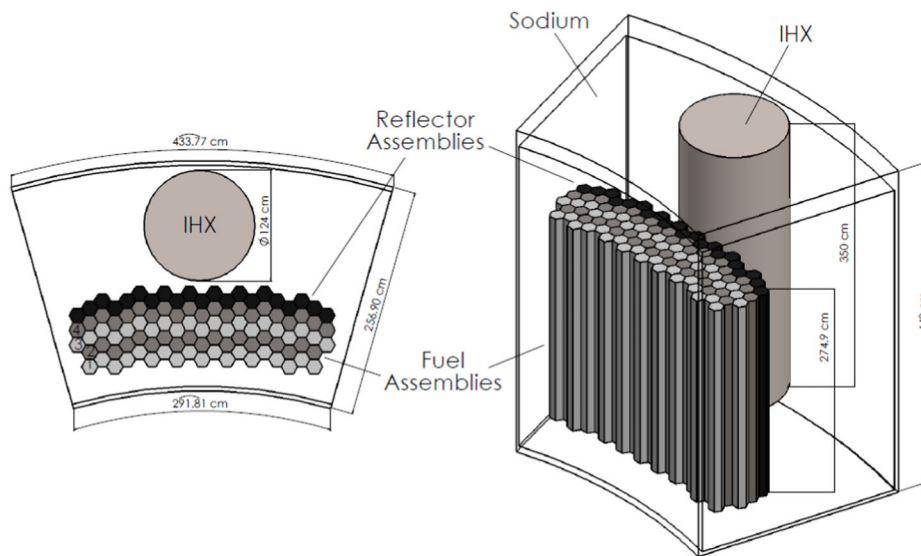


Fig. 5. SABR modular sodium pool configuration.

tapered bottom; these curves are omitted from Figs. 4 and 5 for simplicity.

Each modular sodium pool contains 80 fuel assemblies in four radial layers of (from in to out radially) 19, 19, 21, and 21 assemblies; there is one layer of 21 reflector assemblies outside the fourth radial layer of fuel assemblies. The layout of the fuel assemblies and the IHX within each modular pool is shown in Fig. 5. Each sodium pool also contains two electromagnetic pumps.

We plan in future dynamic safety studies to examine the neutronic coupling of the modular sodium pools for the possibility of power oscillations. We anticipate that the modules will be tightly coupled and any incipient power oscillations would be strongly damped, but we plan to examine this matter.

III.C. SABR Refueling

The sodium pool removal ports are located at pools numbered 1 and 6 in Fig. 4. After removing pools 1 and 6, the remaining pools in each bank can be rotated through the annulus to their respective removal position and extracted. Pools 1 through 5 are removed through refueling port 1, and pools 6 through 10 are removed through refueling port 6. Reloading the modular pools is the reverse of the removal process.

The removal motion can be broken into two distinct phases: the rotation around the annulus and the extraction from within the coils. Because the entire reactor resides within the cryostat under vacuum, there is no access to a secondary heat sink while a pool is in motion. The sodium pool must be disconnected from the secondary coolant and any piped reactor vessel auxiliary cooling system (RVACS). Thus, the only heat removal is by radiative cooling, which is insignificant compared to initial decay heat levels. Therefore, to prevent cladding temperatures from becoming too high while the pool is being moved, the secondary sodium is used to reduce the pool temperature to slightly above the sodium freezing point (378 K) before disconnecting the secondary feed to the IHX. The thermal capacity of the pool is then used to absorb the decay heat while the pool is being moved.

The maximum duration of the rotation phase occurs when pools 5 and 10 are being moved. It is estimated that these rotations will take ~ 1 h. The maximum decay heat rate that could be tolerated without any heat sink for 1 h without clad damage would be 3.18 MW ($\sim 1\%$ of full power). We estimate that reduction to 1% full power occurs in $\sim 10^4$ s, so it should be safe to disconnect the secondary system by 3 h after shutdown. Thus, reduction of decay heat to acceptable levels should not cause any delay in refueling.

Once each pool is rotated around to its extraction point, the secondary coolant feed previously connected to pool 1 (or pool 6) is attached to reduce the temperature within the pool. When a sufficient thermal buffer is re-established, the feed is disconnected and the extraction is

performed. Once a pool is removed from within the coils, it is reattached to a peripheral secondary coolant feed (away from the reactor) to help remove decay heat. The pool is then relocated to a hot cell where the assemblies are removed and the fuel can be sent for reprocessing. Circulation of an inert gas against the sodium pool vessel also becomes available to cool the modular sodium pools once they are outside the cryostat.

It should be noted that neither the heating/current drive apparatus nor the wedge-shaped tritium blankets need to be able to move to facilitate refueling.

Because of the high fast neutron fluence to the plasma-facing pool wall, once every 10 to 15 years, the fresh fuel will be loaded into new pools, which are inserted into the reactor. The exact lifetime of the sodium pool will depend on the irradiation time of each core batch and fuel shuffling, which determine the fusion power. The irradiation time will also influence the amount of cooling time necessary to reduce decay heat levels to 1% of full power.

III.D. Core Neutronics Performance

For the neutronics design analysis, the reactor was represented with a multigroup, finite difference, discrete ordinates approximation in R-Z geometry since all of the structures except for those in the fission annulus have 360-deg symmetry about the toroidal axis. All of the structures within the modular sodium pools were homogenized and given smeared volume fractions that included the core (or reflector) assembly, sodium, vessel wall, and the gaps between the banks of pools. The volume fractions for each radial pool zone are given in Table IV for the original region of the ring, showing how much steel, sodium, and void were smeared into those regions. Because smearing around the annulus effectively dilutes the fuel with small amounts of structure and coolant and spreads it over a larger volume than it truly occupies, it is expected that the spectrum will slightly harden and the reactivity of the fuel slightly increase when modeled in a more precise manner, but this effect is expected to be small.

The R-Z model is shown in Fig. 6, with dimensions given in Fig. 1b. The neutronics calculations were carried out using ERANOS (European Reactor ANalysis Optimized calculation System), a fast reactor code²⁸ originally developed to model the Phénix and SuperPhénix reactors. ERANOS employs the European Cell COde (ECCO) to collapse 1968-group JEFF2.0 cross sections within each reactor lattice cell to the 33 groups used in core calculations, ranging from 20 MeV down to 0.1 eV. The core calculations were carried out using an S_8 quadrature with 170 radial and 292 axial meshes. The fusion neutron source was distributed among 24 plasma regions and grouped into 5 source strengths to approximate the fusion density distribution of a tokamak plasma.

The beginning-of-life (BOL) reactor core characteristics are shown in Table V. The parameter k_{source} is the

TABLE IV
Sodium Pool Radial Ring Volume Fractions for R-Z Model

Radial Zone	Percent Assembly	Percent ODS Steel	Percent Sodium	Percent Void
Inner/outer pool wall	0	87.944	0	12.056
Radially inner sodium	0	2.947	84.997	12.056
Core ring 1	76.167	2.868	8.909	12.056
Core ring 2	74.015	2.787	11.143	12.056
Core ring 3	79.557	2.710	5.677	12.056
Core ring 4	77.429	2.638	7.878	12.056
Reflector ring	0	58.829	24.176	12.056
Radially outer sodium	0	2.261	85.683	12.056

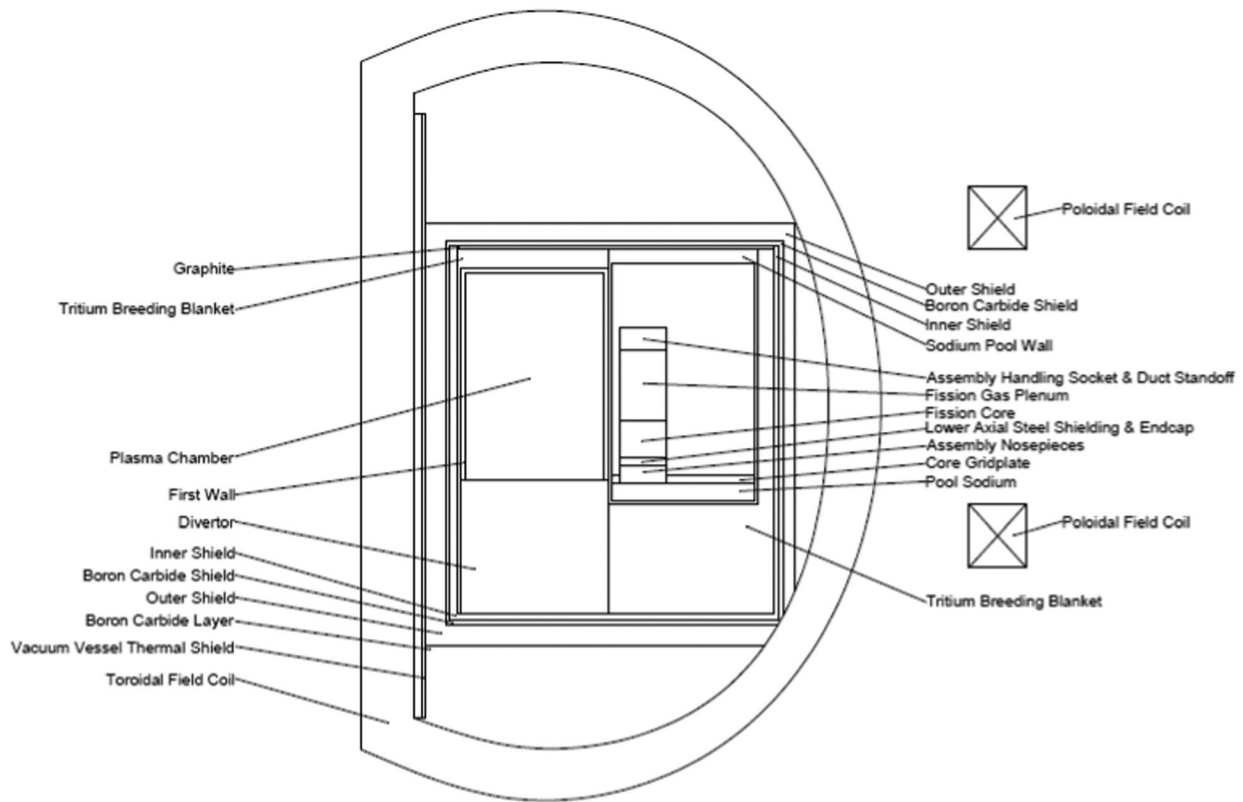


Fig. 6. SABR R-Z neutronics model.

number of neutrons produced on average from each fusion source neutron. Thus, the fusion power required to drive the subcritical fission reaction at a given power level is

$$P_{fus} = P_{fis} \left(\frac{1 - k_{source}}{k_{source}} \right) \nu \left(\frac{E_{fus}}{E_{fis}} \right), \quad (1)$$

where ν is the number of neutrons per fission and E is the amount of energy released per fission or fusion. Table V also shows the more familiar parameter k_{eff} , the number

TABLE V
BOL Core Performance Parameters

Parameter	Value
k_{eff}	0.973
k_{source}	0.756
Fission power [MW(thermal)]	3000
Fusion power [MW(thermal)]	233
Average linear power (kW/m)	12.30
Power peaking (volumetric)	1.27

of neutrons that would be produced on average from each fission neutron if the neutron fission distribution was the same as would exist in a critical reactor, which is different from the neutron fission distribution in a subcritical reactor with a neutron source.

Results from the previous SABR fuel cycle analysis^{20,21} indicate that the limiting factor on fuel residence time with a 500-MW(thermal) neutron source is radiation damage to the cladding. Because the present SABR design includes both a thicker first wall and the sodium vessel wall between the neutron source and the fission core, it may be necessary to extend the fusion neutron source somewhat beyond 500 MW(thermal) to provide 3000 MW(thermal) of fission power to an end of cycle determined by cladding radiation damage limits. (As discussed in Sec. IV, the fusion power level could be increased without changing the design.) The goal of the fuel cycle analysis is to optimize fuel burnup subject to radiation damage to the clad, tritium production, and fusion power constraints. The challenge is in finding a balance among these constraints while matching the refueling window with both the first-wall replacement and the sodium pool replacement intervals to maximize the capacity factor.

III.E. Fast Reactor Thermal Performance

In each of the ten modular sodium pools, 300 MW(thermal) of power is generated. This power is removed by ten shell-and-tube IHXs (one per sodium pool) located beside the fuel assemblies in the sodium pool. The IHX is based on the S-PRISM (Refs. 16 and 29) design and has been shortened to fit into the pool, while preserving the heat transfer rate. Each pool has its own heat exchanger with sodium as the secondary coolant. There are two independent secondary loops, each containing steam generators, turbines, and heat rejection systems that service five of the ten modular sodium pools. The intermediate, steam generator, and heat rejection loops have not been examined in any detail at this stage, because it is assumed that these systems will exist far outside the tokamak and thus will not deviate from existing fast reactor plant designs.

Steady-state thermal-hydraulic calculations for the core and IHX were made using RELAP5-3D (Ref. 30). RELAP solves the multidimensional fluid energy and momentum equations as well as the heat conduction equation to generate the temperature distributions within the core and heat exchanger. A summary of core thermal parameters is given in Table VI, and a summary of heat exchanger parameters is given in Table VII.

One of the purposes of this SABR design activity is to provide a basis for a comprehensive dynamic safety analysis, which will be performed in the near future. However, based on the core design, some preliminary

TABLE VI

Modular Fast Reactor Thermal Performance Parameters

Thermal power per pool	300 MW
Mass flow rate per pool	1669 kg/s
Coolant	Na
Mass of sodium per pool	22 067 kg
Pumping power per pool	20 MW
Number of pumps per pool	2
Pump type	Electromagnetic
Power density	256.7 kW/ℓ
Average linear power	12.3 kW/m
Power peaking	1.27
Core inlet/outlet temperature	628/769 K
Fuel maximum/allowable temperature	1014/1200 K
Cladding maximum/allowable temperature	814/973 K
Coolant maximum/allowable temperature	787/1156 K

TABLE VII

Intermediate Heat Exchanger Parameters

Secondary mass flow rate	1573 kg/s
Secondary fluid	Na
Secondary inlet/outlet temperature (IHX)	590/739 K
Length	3.5 m
Number of tubes	5700
Inner/outer radii of tubes	8.7/9.5 mm

natural circulation calculations were made using the methodology outlined by Todreas and Kazimi.³¹ This requires solving Eq. (2) for the maximum heat removal rate Q from each pool:

$$Q = c_p \left(\frac{2\beta\Delta L\rho^2}{R} \right)^{\left(\frac{1}{2-n}\right)} (\Delta T)^{\left(\frac{3-n}{2-n}\right)}, \quad (2)$$

where

c_p = average specific heat capacity of Na

β = thermal expansion coefficient of Na

g = acceleration due to gravity

ΔL = height difference between core center and heat exchanger center

ρ = cold-leg Na density

R = hydraulic resistance coefficient

n = flow regime ($n = 1$ for laminar, $n = 0.2$ for turbulent)

ΔT = temperature difference across the core.

Natural circulation removes a maximum of 79.4 MW per pool when two conditions are met: (a) the primary sodium in the hot leg is allowed to reach near-boiling temperature of 1150 K and (b) the mass flow rate on the secondary side is maintained at its normal steady-state value. This ensures SABR is passively safe for only certain types of transients. To maintain passive safety in all conditions, a RVACS needs to be designed.

IV. TOKAMAK NEUTRON SOURCE

IV.A. Plasma Physics Parameters

A D-T tokamak based on the physics and technology of the ITER design^{17,18} is used as the neutron source for SABR. A systems code for fusion parameter trade-off studies, based on engineering and physics constraints³² (and used in previous design iterations of the SABR neutron source³³) was used to explore the SABR plasma physics design parameter space. The target maximum fusion power for the tokamak neutron source was chosen to be similar to the ITER design value of 500 MW(thermal). With a target plasma current of 10 MA (chosen based on the previous SABR design), a major radius of 4.0 m was found to satisfy the various engineering and physics constraints, as well as provide a flexible operating physics parameter range.

Systems studies were performed to determine the values of normalized beta (plasma to magnetic pressure

ratio), auxiliary H&CD power, and confinement H-factor [multiplier on the empirical ITER IPB98(y,2) confinement scaling] required to achieve various fusion power outputs at $R = 4.0$ m, $I = 10$ MA, and $B_\phi = 5.6$ T. The normalized ratio of plasma pressure to the magnetic pressure β_N was varied between a conservative value of 3% (routinely exceeded in present experiments) and a moderately improved value of 4% (often exceeded in present experiments). The upper limit of achievable β_N is determined by plasma MHD stability limits with respect to ballooning modes. The confinement scaling parameter H-factor is a measure of the enhancement of energy confinement time compared to the ITER IPB98(y,2) empirical scaling law of present tokamak confinement values as of 1998 and was varied in the conservative range of 1.0 to 1.4 that has been achieved since that time. As shown in Fig. 7, there is a rather wide range of plasma physics operating space within which the target design parameters can be achieved. We select as reference design parameters [500 MW(thermal) fusion power, H-factor = 1.2, $\beta_N = 3.2\%$], for which the reference auxiliary heating power is 110 MW(thermal), with a corresponding $Q_p = P_{fus}/P_{aux} = 4.6$.

Looking at the operational space in a different way, Fig. 8 displays the major radius, plasma current, and fusion power phase-space that can be accessed for a plasma with minor radius $a = 1.2$ m, H-factor = 1.2, and $\beta_N = 3.2\%$.

The design parameters and constraints are summarized in Table VIII. The values in parentheses indicate the range of these parameters for which a neutron source design meeting the SABR requirements could be achieved, based on Figs. 7 and 8.

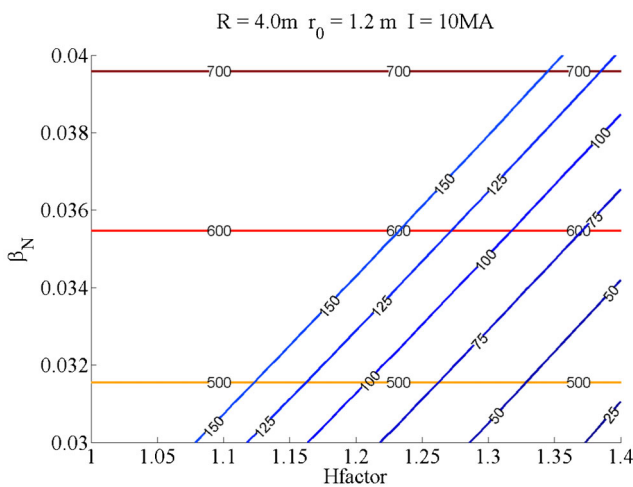


Fig. 7. H-factor, β_N , auxiliary power, and fusion power operational space for SABR. (The horizontal lines indicate the fusion power, and the slanting lines indicate the H&CD power in megawatts. $B_\phi = 5.6$ T.)

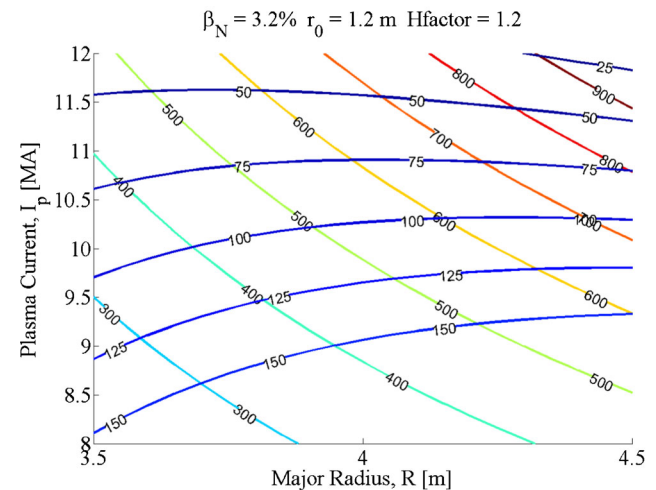


Fig. 8. Major radius and plasma current phase-space for SABR. (The contours of constant fusion power are shown by the lines going from upper left to lower right, while the H&CD power contours go from lower left to upper right. $B_\phi = 5.6$ T.)

TABLE VIII

 Tokamak Neutron Source Plasma Physics Design
Parameters and Constraints

Variable	Value
TF in plasma	5.6 T
Flux swing in CS	26.3 V·s
CS magnetic field	13.5 T
Elongation, κ	1.5
Triangularity, δ	0.4
Safety factor at 95% flux surface	3.0
Safety factor at centerline	1.0
Fraction of Greenwald density	0.75
Power output	500 MW
Auxiliary heating power	110 MW
Bootstrap current fraction	0.55
Minor radius	1.2 m
Fusion power gain, Q	4.6
Major radius	4.0 (3.5 to 4.5) m
Plasma current	10 (8.0 to 12.0) MA
Confinement H-factor	1.2 (1.0 to 1.4)
Normalized beta β_N	3.2% (3.0% to 4.0%)
Average density	$1.65 \times 10^{20} \text{ m}^{-3}$
Average temperature	12 keV
Neutron source rate	$\leq 1.8 \times 10^{20} \text{ n/s}$
Inductive startup flux fraction	0.60

These parameters are for the most part conservative, in that they have already been achieved and will be demonstrated in ITER operation. The bootstrap current fraction was taken to be constrained at 55%, which is a reasonable value according to previous analysis for ITER (Ref. 34), ARIES (Ref. 35), or other advanced plasma scenarios.³⁶ Perhaps the most aggressive design assumption in this analysis is that 40% of the noninductive current drive will be obtained through electron cyclotron (EC) and radio-frequency (RF) current drive technology, which is discussed in Sec. IV.B.

IV.B. Plasma H&CD Systems

IV.B.1. H&CD System Design Considerations

The objective of the H&CD systems design is to use the same H&CD systems that will be demonstrated on ITER, insofar as possible. The unique geometric restrictions imposed on SABR by the presence of the annular fission core within the TF coil system, along with economic considerations, discouraged the use of the large neutral beam and ion cyclotron (IC) H&CD systems, thus guiding the design toward the utilization of the smaller EC and lower hybrid (LH) H&CD systems. LH and EC systems are known to drive current efficiently,³⁶⁻³⁸ providing the necessary noninductive current drive for steady-state operation and startup assistance.³⁹

The design analysis of the H&CD system began with an examination of the constraints and limits that would be faced in its implementation. The main challenge for a H&CD system on SABR is the limited midplane plasma access on the outboard side of the tokamak because of the presence of the surrounding annular reactor core within the TF coils. The ITER H&CD system design specifies modular, horizontally inserted port plugs interfacing with the plasma at the outboard midplane that can carry EC, LH, and IC systems, plus additional EC systems in the upper outboard quadrant,⁴⁰ a location much more easily accommodated in the SABR design than midplane access. LH systems, on the other hand, have not been shown to have launch angle flexibility and conservatively have outer midplane plasma access.

In SABR, two H&CD access ports ($\sim 1\text{-m}$ toroidal arc length and full plasma height at the first wall) will bring the H&CD power into the plasma. These ports will be 180 deg apart toroidally and will pass between adjacent Na pools (see Fig. 4). The radial extent of the Na pool and access requirements for the associated refueling equipment also limit the azimuthal launch angles of the outboard midplane H&CD systems.

There are two requirements on the H&CD system. The first is to start up the 10 MA of plasma current, and the second is to maintain that plasma current indefinitely in steady state. The current can be started up by a combination of (a) inductive magnetic flux swings provided by the central solenoid (CS) and the PF coils and (b) by noninductive startup assist provided by the H&CD system.

An important requirement of the H&CD system for the SABR design is to noninductively drive a plasma current of 4.5 MA, which supplements the 5.5 MA of bootstrap current to provide 10 MA of plasma current. Analyses like those leading to Figs. 7 and 8 show that the auxiliary power input levels necessary to operate at a sufficient fusion power are within the capabilities of an ITER-like H&CD system,⁴⁰ allowing a focus here on integration of current drive capabilities into the SABR design. An ideal current drive system would also drive controllable current profiles and be capable of stabilizing neoclassical tearing modes⁴¹ (NTMs), which requires steerable EC launchers.

IV.B.2. Current Drive Efficiency and Profile Control

An expression for the current drive efficiency of a RF system commonly used in the literature is

$$\gamma_{CD} = \frac{n_{20} R_m I_A}{P_w}, \quad (3)$$

where

n_{20} = electron density of the plasma ($10^{20}/\text{m}^3$)

R_m = major radius (m)

I_A = driven plasma current (amps)

P_w = RF power (W).

The SABR neutron source plasma requires 110 MW of auxiliary power to drive 4.7 MA of current in the plasma. In analyses of the DEMO (Ref. 38) and ITER (Ref. 37) facilities, it has been shown that current drive efficiency values of ~ 0.035 and 0.025 A/W can conservatively be expected from LH and EC systems, respectively, during operation in advanced plasma scenarios that will be investigated on ITER. This research suggests that a system of 40 MW of LH power plus 70 MW of EC power could meet the noninductive H&CD requirements of SABR, based on the design value of average plasma electron density of $\sim 1.65 \times 10^{20} \text{ m}^{-3}$.

One common goal of current drive systems is to enable a controllable current drive profile, and modeling^{36,40} suggests that this may be realistically achievable to some degree with a combination of EC and LH H&CD. Lower hybrid current drive and bootstrap current tend to concentrate toward the plasma boundary,^{36,37} peaking the current drive profile. Analysis of ITER scenarios⁴⁰ and scenarios of proposed research facilities³⁶ show that the radial deposition of current drive from EC systems can be modified by changing the azimuthal launch angle of the EC wave, at the cost of efficiency. At peak efficiency and with a bootstrap current fraction of 55%, the current drive of the system proposed in the previous paragraph would drive an additional 200 kA of current above the nominal 4.5 MA required driven plasma current of the design. Although this excess current may have some benefits, a trade-off could be made between overcapacity and configuration of the current drive profile by altering the azimuth of the incoming EC waves, and driving current less efficiently at more favorable radial locations, as illustrated by Fig. 9 in Ref. 36. This type of design consideration could mitigate the peaking associated with the current drive of LH systems and the bootstrap phenomena.

IV.B.3. H&CD System Plasma Access and Geometric Analysis

The EC and LH H&CD systems use the modules developed for use in ITER (Ref. 40), with a minimal level of modification required. The 40 MW of LH H&CD will comprise two 20-MW LH units with launchers centered about or slightly below the outer midplane of the two access ports 180 deg apart. This system will comprise the same power supply, transmission line, and launcher units as those of the modular LH H&CD port plug designed for use in ITER. Also, 40 MW of the EC H&CD power will be provided by two 20-MW systems using the ITER equatorial port plug components, launching through the two main H&CD access ports. The EC units will be installed above the LH ports, and the launchers will

vertically follow the curvature of the plasma and first wall, with a poloidal position ranging from above the near-midplane LH H&CD units through the upper quadrant location. This location is beneficial for geometric considerations and provides some ancillary benefit to the EC current drive efficiency, as analysis³⁸ suggests that efficiency is higher when the waves are launched from the upper quadrant.

A redesign of the ITER EC H&CD systems to conform to the geometry of the main SABR H&CD access ports instead of those for ITER could allow the full amount of EC H&CD power envisioned for SABR to be launched from the main access ports, if this should prove to be beneficial. Although the minimization of the number of upper quadrant ports is desirable in the SABR design, it may be important to include at least two steerable upper quadrant launchers (located toroidally between the main access ports) for use in stabilizing NTMs. For the LH and EC H&CD launchers located in the main access ports, we anticipate some reduction in the necessary geometric size of the concatenation of the two launchers due to a consolidation and reduction in the amount of shielding.

Since the SABR design has a smaller plasma and the plasma access is limited by the surrounding annular fission core, a reexamination of the design of the ITER port plugs and upper quadrant plugs should be undertaken for the purpose of minimizing their size. The ITER equatorial port plugs are designed to accommodate large ICRF launchers, which are not planned for SABR. Moreover, with the comparatively higher launcher power density capabilities of the EC and LH H&CD technologies, it is reasonable to believe that the size of the modular equatorial port plugs could be reduced to fit the main SABR port geometries and still support a RF system consisting solely of LH and EC H&CD. The ITER upper quadrant EC H&CD port width tapers significantly toward the plasma, and it would be favorable to the SABR design, but not mandatory, if this port design was more refined so that the maximum cross section was more closely approximated by the section nearest to the plasma, rather than the large support plate in the ITER design. The geometric implementation of the RF H&CD systems for SABR will have to be engineered when the overall design is developed in greater detail, but the specifications of the SABR system seem to be well within realistic parameters achievable with ITER LH and EC H&CD system components.

The upper quadrant port designs for ITER incorporate steerable 7-MW EC H&CD systems,⁴⁰ and the remaining EC H&CD power not launched from the midplane access ports will be evenly distributed toroidally in the upper outboard quadrant positions between the main access ports to provide steerable H&CD and NTM stabilization capability. Using the ITER components for all launchers, this would suggest that four 7-MW upper quadrant

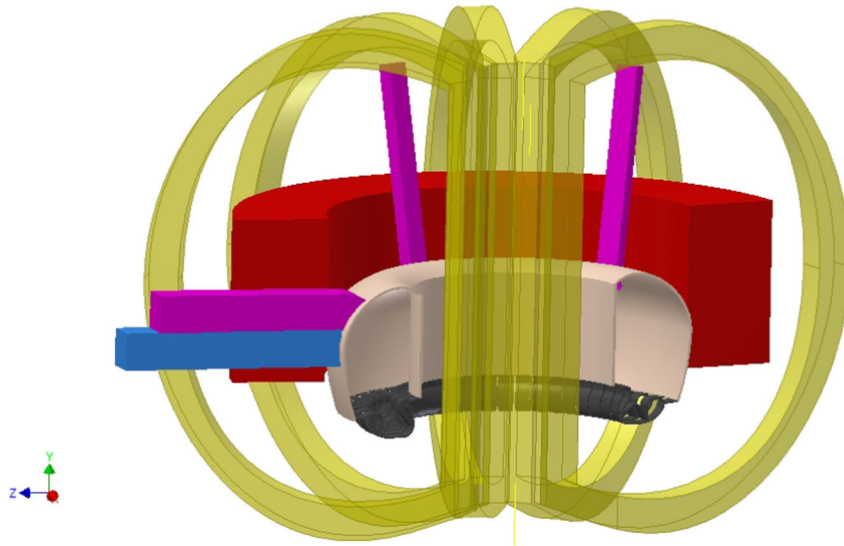


Fig. 9. Possible H&CD configuration. [On the left are one of two 20-MW LH equatorial (bottom) and 20-MW EC “high-equatorial” launchers in the H&CD port. In the center are two of the four 7-MW EC upper quadrant launchers shown accessing the plasma vertically from above. For clarity, only half of the plasma chamber, sodium pool annulus, and TF coils are shown. The shielding, structure, and tritium blankets are omitted.]

launchers would be included, with two in each area between access ports. To accommodate the upper quadrant plasma access restriction provided by the modular sodium pools in SABR, some reconfiguration of the geometry of components in the 7-MW EC launchers may be needed, e.g., reducing the angle between the axes of the CS and the launcher, while maintaining the same poloidal location of the launching window as in the ITER design. One possible adaptation of the ITER H&CD system is shown in Fig. 9.

IV.B.4. H&CD System Noninductive Startup Assistance

Noninductive startup of tokamak plasmas has long been a goal of fusion researchers, due to the geometric, economic, and performance benefits that would result from the reduction or even removal of the CS magnet system. In present tokamaks, the PF coils and CS provide the magnetic flux required to start up and drive the toroidal current (which heats the plasma ohmically). The CS of the SABR tokamak neutron source provides $\sim 60\%$ of the total magnetic flux necessary to initiate full plasma current, requiring the assistance of the PF coils and the noninductive H&CD system to bring the plasma current to its full value of 10 MA.

Thus, another function of noninductive H&CD is to assist with current startup by reducing the amount of magnetic flux that would otherwise be required from the magnet systems to achieve 100% inductive startup. This use of the H&CD system also improves confinement during low-confinement mode and facilitates the low to high confinement mode transition by shaping the safety factor profile.⁴² The LH H&CD system plays a crucial

role in startup “flux saving” and also has other, more specific, benefits, such as enhancing plasma control during startup.⁴³ It is especially efficient at current drive early in the discharge, after dissociation and before the density increases to operational values, driving current near the plasma center and favorably impacting stability.⁴⁴

An investigation by Kim et al.⁴³ found that in ITER-like plasmas, a large majority of plasma current will be driven by the LH system until almost half of the 15-MA ITER plasma current is achieved at 38 s, where the LH-driven plasma current reaches its maximum during startup. This analysis was performed with 20 MW of LH power. Hogweij et al.⁴⁴ estimate that for flux consumption “a reduction of $\sim 15\%$ can be reached,” while in the analysis by Kim et al.,⁴³ early application of LH power resulted in a flux savings of 43 Wb out of 124 Wb for the control discharge without LH startup assist. The flux that is expected to be provided from the ITER CS is ~ 118 Wb (not including the contribution from the PF coils^{40,45}).

Results from the examination of using EC H&CD in startup control are also promising,³⁹ and it has been used successfully for various purposes on low-aspect-ratio devices, e.g., in a simulation of the planned NSTX-U during startup.^{46,47} It also seems to be effective in assisting startup by minimizing flux consumption, increasing plasma control, and enabling better hybrid scenarios on larger machines like DIII-D (Ref. 39), Tore-Supra (Ref. 48), and in ITER scenarios.⁴²

The application of similar analyses to the plasma regimes of SABR remains to be done, but given the above results, the ability of the LH and EC H&CD systems of

TABLE IX
SABR H&CD System Parameters

EC power	70 MW, two 20-MW units and four 7.25-MW units	LH power	40 MW, two 20-MW units
EC current drive efficiency	0.025 A/W	LH current drive efficiency	0.035 A/W
EC frequency	170 GHz	LH frequency	5 GHz
Average plasma, n_e	$1.65 \times 10^{20} \text{ m}^{-3}$	Required steady-state current drive	4.5 MA
Maximum required noninductive current drive for startup	4 MA	Excess steady-state current drive for profile shaping	200 kA
Maximum available inductive current drive for startup	6 MA (CS only)	Total steady-state current drive	4.7 MA

SABR to complement the flux generation of the PF and CS and enable full plasma current startup seems feasible.

For the SABR tokamak neutron source, the CS is designed to induce 6 MA of current during startup, and the noninductive current drive will be expected to contribute ~ 4 MA. This inductive and noninductive plasma current driven during startup totals the 10 MA of plasma current specified in the design. As fusion heating occurs and the bootstrap current engages, the noninductive current drive system will ramp to its full capacity. The flux contributed by the current ramp in the PF coils will also provide a significant inductive contribution to current startup, which is not taken into account in the above considerations. This excess current startup capability will allow the noninductive current drive system to further tailor plasma safety factor profiles, as is done in the hybrid startup scenarios,⁴² or will allow the noninductive system to stand by to provide additional current as needed. Several important parameters of the H&CD system are listed in Table IX.

IV.C. Magnet Systems

IV.C.1. Toroidal Field Coils

Tokamak reactors confine plasma using superimposed toroidal and poloidal magnetic fields. Large TFs are necessary to stabilize the plasma against MHD “kink” instabilities and other instabilities that would be deleterious to plasma performance. These large fields are generated by a series of D-shaped TF coils outside of the plasma.

The ITER superconducting (SC) TF coil system⁴⁹ shown in Fig. 10 has been used, with very few modifications, for the upgraded SABR design. The same coil dimensions, “cable-in-conduit” conductor design, coil structural design, etc., are used. Each ITER TF coil is capable of carrying 9.13 MA of current and generating a maximum field of 11.8 T at the conductor. The SABR TF coils are the same size as the ITER coils but are reduced in number from 18 to 10 (to provide access for refueling) and are located at a smaller major radius (because of the reduction in size of the CS for SABR relative to ITER). The SABR TF coils produce the same 11.8 T maximum

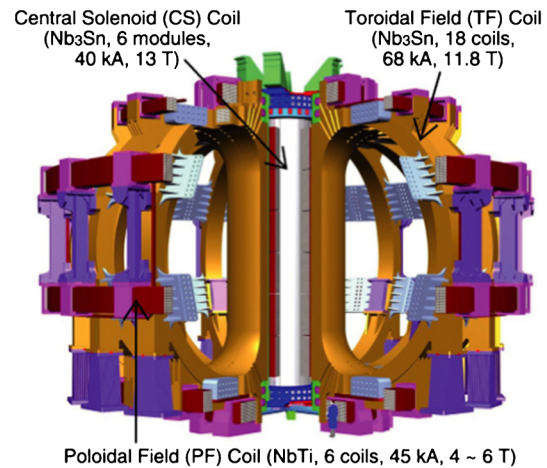


Fig. 10. The ITER SC magnet system.¹⁸

field at the conductor as in ITER with a slightly larger current of 11.2 MA per coil. The SABR coils, like the ITER coils, are helium-cooled through channels inside the conductor windings and are thermally insulated from the reactor by actively cooled thermal shields.

Since SABR incorporates only 10 TF coils, compared to 18 TF coils in ITER, it might be expected that the field ripple on the outboard of the plasma would be larger than in ITER. However, since the SABR plasma diameter of 2.4 m is much less than the ITER plasma diameter of 4 m, the outboard surface of the plasma is 1.6 m farther from the outboard leg of the TF coil in SABR than in ITER. This probably more than compensates for the increase in field ripple at the outer plasma surface that would be produced by reducing the number of TF coils from 18 to 10. If not, ferromagnetic inserts can be added on the inboard side of the outer leg of the TF coil⁵⁰ to correct any significant field ripple.

IV.C.2. Central Solenoid and PF Coils

The poloidal field that confines the plasma is generated by a current in the plasma itself. In ITER and most modern tokamak designs, this current is initiated and, to some extent, controlled using a CS and a set of PF

coils. These coils, in addition to a series of smaller correctional coils around the plasma, are also instrumental in controlling the shape and vertical position of the plasma.

The CS design of SABR is adapted from the ITER design.⁴⁹ In SABR, the CS is designed to provide 60% of the inductive flux swing necessary for startup. The remaining 40% will be provided by a combination of the inductive flux swing from the PF coils and noninductive current drive methods. The SABR CS is designed to produce 59 Wb to induce 6.0 MA of inductive plasma current for startup. With a maximum field of 13.5 T in the CS magnet, this flux swing requires a flux core radius of 0.69 m. To satisfy a stress limit of 200 MPa, the CS coil thickness must be 0.3 m thick.

The PF coil system is anticipated to be essentially identical to that of ITER (Ref. 49) shown in Fig. 10, although the currents and perhaps the locations may be altered to accommodate the smaller SABR plasma and plasma current. The vertical separation of the ITER PF coils nearest the outboard midplane allows a vertical distance of 4.4 m for removal of the fission core Na pool modules. The pool modules in SABR were designed to be no more than 4.4 m tall, which is the approximate distance between PF3 and PF4 on ITER. It should be possible to adjust the ring coil positions to achieve a somewhat larger vertical opening for Na pool removal, if necessary.

IV.D. Divertor and First Wall

Energetic particles leaving the last closed flux surface of the plasma are swept downward toward either the inboard or outboard divertor targets and deposited over a

relatively small area. Energetic photons from bremsstrahlung, line and recombination radiation, and atomic physics processes in the plasma are distributed uniformly over the plasma chamber first wall as a surface heat flux. In addition, there is a power flux of 14-MeV neutrons and lower-energy fission neutrons through the first wall, some of which are deposited as a volumetric heat source. At full fusion power of 500 MW and full H&CD power of 110 MW, there will be 210 MW of non-neutron power emerging from the plasma. Assuming that this emerging power is equally distributed between photons (radiation) and charged particles, this will constitute a power flow to the divertor of 105 MW and an average surface heat flux to the first wall of 0.44 MW/m². It is possible to increase the radiation fraction of the power leaving the plasma by injection of impurity ions in the edge, and ITER uses this scheme to achieve a 15/85 split between charged particle and radiation. This same split would result in a power flow to the divertor of 31.5 MW and an average surface heat flux on the first wall of 0.74 MW/m². The average power flux of 14.1-MeV fusion neutrons through the first wall is 1.7 MW/m², and the scattered fusion neutron plus fission neutron power flux through the first wall is 0.6 MW/m².

IV.D.1. Divertor

The toroidal divertor for SABR was adapted⁷ from the ITER divertor (Fig. 11) to sodium coolant and a somewhat smaller plasma major radius. It comprises a series of divertor cassettes that allow for the radial removal of individual divertor modules through horizontal divertor ports below the sodium pools for maintenance

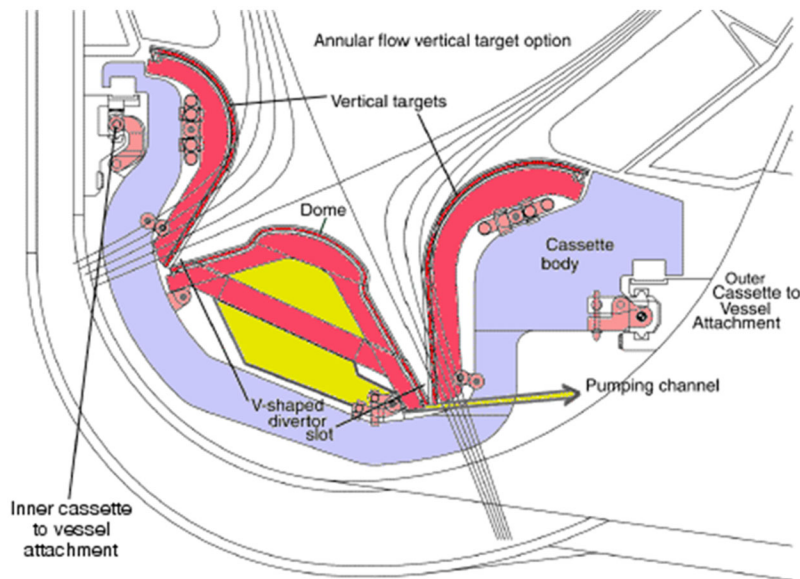


Fig. 11. ITER divertor plasma heat sink.¹⁸

and replacement. The SABR divertor and first wall are cooled by the same 10-mm coolant channel structure as in the ITER design, but with sodium coolant. These channels are lined with thin layers of SiC to mitigate MHD pressure drops.

Detailed heat removal calculations previously carried out for the ITER divertor cooled with sodium⁷ indicated that the heat removal capability was more than adequate. The heat removal system was modeled using Fluent,⁵¹ a three-dimensional fluid program that solves the energy equation coupled with the Navier-Stokes equation. The Fluent model and mesh were created for a single cooling channel. For an inlet coolant temperature of 293°C, the maximum CuCrZr temperature is 756°C, well below the 1500°C melting point of CuCrZr.

The smaller total surface area of the divertor in the SABR design than in the ITER design, together with similar anticipated incident total energy loads, will increase the heat load per unit area of the divertor (and on the first wall) for SABR relative to ITER. Based on the previous analysis,⁷ we believe that heat removal from the SABR divertor will be adequate, but this will be checked again in the future.

IV.D.2. First Wall

The first wall consists of the plasma-facing components of the containment vessel with their associated coolant channels. The materials used in the first wall must be resilient against extreme heat and particle fluxes. Although most current tokamaks incorporate carbon tiles in the first wall, ITER will use 8.1-cm-thick beryllium-clad ODS steel. While reductions in first-wall thickness are anticipated in post-ITER tokamaks, SABR incorporates the ITER first-wall design but with sodium as the coolant.

The SABR first-wall design anticipates average heat loads of ~ 0.44 MW/m², again, based on a roughly 50/50 split between radiated power and charged particles leaving the plasma and assuming 500-MW fusion power. As in ITER, certain panels used as limiters during startup will be exposed to significantly higher loads and will make use of enhanced panels. Although higher than average ITER heat loads of ~ 0.25 MW/m², this average heat load is well below the design tolerances of the approved ITER first-wall panel designs (2 MW/m² for normal panels and 4.7 MW/m² for enhanced panels). The melting point of beryllium imposes an upper limit on the allowable temperature under accident conditions of 1200°C. As with the divertor, the increased heat and particle flux per unit area over the first wall relative to ITER will be mitigated by the fact that the tiles will be cooled with sodium rather than water. Detailed heat removal calculations for the previous SABR design⁷ indicate more than adequate thermal performance with sodium coolant, with surface temperatures well below the 1200°C design limit necessary to avoid Be melting.

V. TRITIUM BREEDING BLANKET

SABR must at least be tritium self-sufficient (and ideally a tritium producer for the startup of future SABRs), which requires lithium-containing tritium breeding blankets near the fusion source and the neutron multiplying subcritical fast reactor modules. The eight blanket modules used to generate tritium for SABR are (a) the “inboard” blanket (TB1) located just outside the first wall of the plasma chamber on the inboard side; (b) the “plasma” blanket (TB2) located above the plasma core; (c) the “core” blanket (TB3) located below the fission core in regions not occupied by the divertor module replacement ports; (d) the “outboard” blanket (TB4) located radially outboard from the modular sodium pool but inside of the shielding; and (e) four wedge-shaped blankets (TB5 through TB8) that occupy space between the modular sodium pools in the fission annulus, as shown in Fig. 4.

V.A. Configuration and Materials

The blanket is composed of solid lithium orthosilicate (Li₄SiO₄), chosen because of its high lithium atomic density, low chemical reactivity, and relatively wide operating temperature range for tritium recovery. A high lithium atomic density is desirable because of the ⁶Li(*n*,α)T reactions that are utilized to breed tritium for the plasma neutron source. The cross section for the ⁶Li reaction is ~ 650 b for thermal neutrons⁵² and much smaller for ⁷Li; therefore, the analysis performed for tritium production was with a blanket design enriched in ⁶Li to 90%. The tritium produced from these (*n*,α) reactions migrates through the grains of the solid breeding blanket into helium purge channels that carry the tritium away to purification and processing facilities.^{53–56} The purge and sodium coolant channels are arranged in an array format within the tritium breeding blanket, with a pitch-to-diameter ratio of 10 for both types of channels. The operating temperature window for tritium recovery⁵² of Li₄SiO₄ is $T_{min} = 325^\circ\text{C} < T < T_{max} = 925^\circ\text{C}$.

V.B. Tritium Breeding Ratio

Calculations for lithium capture and corresponding tritium production in the blanket were performed for the BOL conditions using the ERANOS fast reactor code²⁸ in conjunction with the neutronics model discussion in Sec. III. The coolant and purge channels were neglected in these calculations due to the small volume fraction compared to the blanket material (<1%), and the calculation was based on one tritium atom produced for every ⁶Li or ⁷Li capture. A useful parameter to characterize tritium self-sufficiency is the tritium breeding ratio (TBR), which is defined as

$$TBR = \frac{\dot{N}_b}{\dot{N}_p}, \quad (4)$$

where \dot{N}_b is the rate of tritium production in the blanket and \dot{N}_p is the rate of tritium burning in the plasma chamber. The TBR must be > 1 by some margin to allow for decay, losses in the processing systems, and restart after maintenance and refueling shutdowns. A typical value used to satisfy this criterion in previous fusion reactor analysis⁵⁶ is 1.15, and a TBR value of 1.12 was calculated for the SABR blanket configuration shown in Figs. 1 and 4. These blankets will be shown subsequently to fulfill the tritium inventory requirements for SABR.

The ERANOS S_8 discrete ordinates calculation of the TBR was checked by comparison with the Monte Carlo neutron transport code⁵⁷ (MCNP) calculation described in Sec. VI. The MCNP calculation of the TBR was $< 5\%$ larger than the ERANOS calculation, with the differences being attributable to slight geometrical differences in the models and to slight differences in the definition of the fusion neutron source.

V.C. Thermal Performance

Tritium migration rates through the solid lithium orthosilicate blanket to the purge channels are dependent upon the operating temperature of the blanket. Most migration occurs for blanket temperatures between 400°C and 900°C (Ref. 52), which is significantly under the melting temperature of 1250°C. A single cell of the sodium coolant tube matrix for the plasma blanket TB2

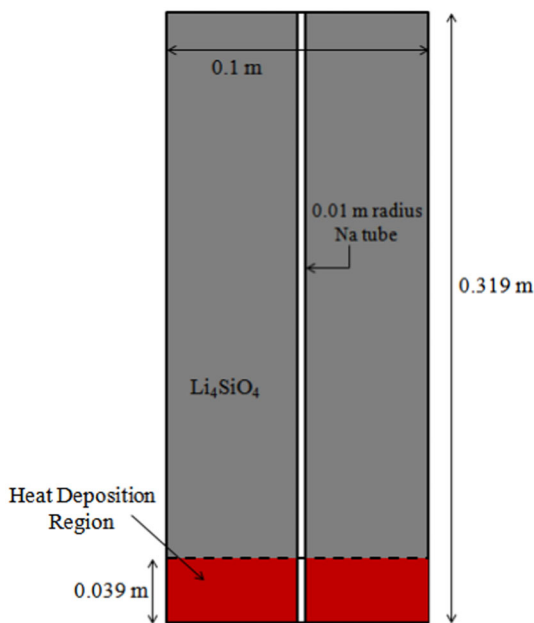


Fig. 12. Schematic of blanket and coolant channel cell for the plasma blanket.

TABLE X

Thermal-Hydraulic Parameters for RELAP5 Model

Parameter	Value
Na inlet temperature	450°C
Hydraulic diameter	0.02 m
Diameter of blanket cell	0.2 m
Na mass flow rate	1 kg/s
Na velocity	3.815 m/s

(Fig. 12), was analyzed using RELAP5 (Ref. 30). Table X summarizes the parameters for the RELAP5 model. Similar calculations were carried out for the similar plasma blanket TB2 and the taller inboard (TB1) and outboard (TB4) blankets.

The coolant channel cell model, with appropriate dimensions, and the thermal-hydraulic parameters in Table X were used to calculate heat removal and temperatures for the four blanket modules TB1 through TB4. The total power generated in each blanket was determined from the ERANOS neutron plus gamma heating calculation, which was assumed to be uniformly deposited in a smaller fraction of the respective blanket close to the neutron source (either plasma or fission) to perform a conservative heat removal analysis. The “heat deposition region” is located at the bottom for the “plasma” module adjacent to the plasma neutrons, the top for the “core” module close to the fission neutron source, and assumed to be uniform over the entire blanket for the “inboard” and “outboard” modules due to their small thicknesses. Assuming that all the power was deposited in this “heat deposition region” as shown for the plasma blanket as an example in Fig. 12, all four blanket modules were determined to be well within the tritium migration window constraint of $T_{min} = 325^\circ\text{C} < T < T_{max} = 925^\circ\text{C}$, as shown in Table XI.

Because of the inappropriateness of the current two-dimensional model representation of the wedge-shaped blanket zones TB5 through TB8, heat removal analysis was not performed for these blankets. Although these blankets contribute just under 6% of the tritium production, they are relatively large and therefore impose less stringent heat removal constraints. Since the smaller blankets with large power densities, such as the inboard tritium blanket (TB1), are shown to be properly cooled with sodium, it is assumed that the wedge-shaped blankets (TB5 through TB8) can also be sufficiently cooled with the present blanket cooling configuration.

V.D. Tritium Recovery and Self-Sufficiency

The value of the TBR is a preliminary check of the SABR capability to produce more tritium than it

TABLE XI
Heat Removal Parameters for the Tritium Blanket Modules

Parameter	Plasma Blanket	Core Blanket	Outboard Blanket	Inboard Blanket
Maximum temperature	574°C	462°C	451°C	491°C
Minimum temperature	450°C	450°C	450°C	450°C
Total power removed	26.1 MW	25.5 MW	9.5 MW	24.1 MW
Power per tube	12 757 W	7550 W	21 316 W	670 378 W
Number of tubes	2050	3373	447	36
Length of blanket	0.319 m	1.9 m	6.3 m	6.3 m
Length of heat deposition	3.98 cm	23.75 cm	Uniformly	Uniformly
Na outlet temperature	451°C	451°C	451°C	479°C

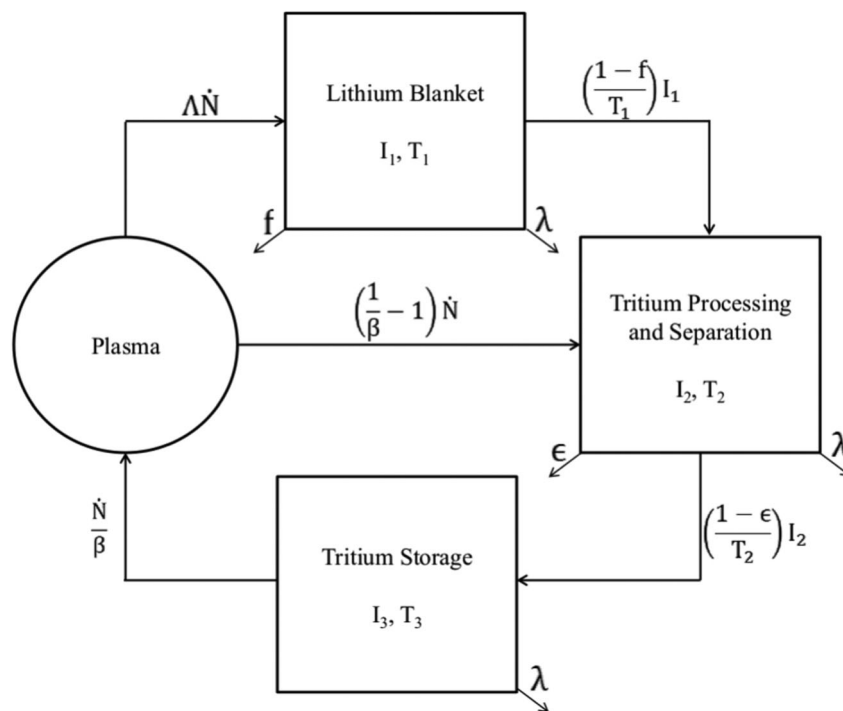


Fig. 13. Schematic of time-dependent tritium inventory model with parameters described in Table XII.

consumes. However, the time dependency of the tritium inventory must be examined to ensure that small unplanned outages of processing systems and large planned shutdowns can be tolerated. Previous analysis⁵⁶ has defined general analytical models to determine the tritium inventory in plasma fusion reactor systems. The SABR system model has been simplified to that shown in Fig. 13 with model parameters defined in Table XII.

Once the fuel cycle is determined, the time-dependent fusion neutron source requirement will be known and can be used in the calculation. For now, we estimate based on past experience that the average fusion power level over the

first year would be ~260 MW and carry out the inventory calculation at this fixed fusion power level over the year.

Equations (5) describe the tritium inventory for the blanket I_1 the processing system I_2 , and the storage containment I_3 . The requirement for the initial inventory in storage to start the fusion reactor was determined by the constraint that $I_3 > 0$:

$$\dot{I}_1 = \Lambda \dot{N} - \frac{I_1}{T_1} - \lambda I_1,$$

$$I_1(0) = 0,$$

TABLE XII

Tritium Inventory Model Parameters

Parameter	Description	Value
\dot{N}	T burn rate in plasma ^a	$9.38 \times 10^{19} \text{ s}^{-1}$
Λ	TBR ^a	1.12
T_1	Residence time in blanket ^b	10 days
T_2	Residence time in T processing ^b	1 day
ε	Nonradioactive loss in processing ^b	0.1%
λ	T decay constant	$1.7841 \times 10^{-9} \text{ s}^{-1}$
f	T leakage from blanket and other nonradioactive loss ^b	1.1%
β	T burn fraction in plasma ^b	5%
I_1	Steady-state T inventory in blanket ^c	0.451 kg
I_2	Steady-state T inventory in processing ^c	0.811 kg
I_3 (1 year)	T inventory in storage ^c after 1 year	1.071 kg
I_0	Required startup inventory ^c	0.7 kg (excluding minimum inventory)
I_{min}	Minimum inventory	2.3 kg

^aERANOS (Ref. 26).

^bPrevious analysis.⁵³

^cEquation (5) and Fig. 12.

$$\dot{I}_2 = \frac{1-\beta}{\beta} \dot{N} + \frac{1-f}{T_2} I_2 - \lambda I_2,$$

$$I_2(0) = 0,$$

$$\dot{I}_3 = \frac{1-\varepsilon}{T_2} I_2 - \frac{\dot{N}}{\beta} - \lambda I_3,$$

and

$$I_3(0) = I_0. \quad (5)$$

Solutions to Eqs. (5) with zero initial tritium concentration for the blanket and the processing system are shown in Fig. 14. With these parameters, the tritium doubling time for the system is ~ 470 days, and the reactor regains the initial inventory amount I_0 again in the storage containment in 250 days. If the reactor runs for 1 year and shuts down for refueling for 90 days, there will be ~ 2.3 kg left, which is enough to restart the reactor with the requirement of 0.7 kg.

The above modeling is more simplistic than in Ref. 53 because plasma exhaust, tritium breeding blanket, tritium breeding blanket coolant, first-wall coolant, and cleanup and separation processing units are lumped into one processing compartment with a composite residence time. During operation, any one of these compartments may be shut down for maintenance, requiring a minimum tritium inventory I_{min} in the storage vessel such that the reactor can continue operation. This minimum inventory depends most on the plasma fueling rate and fractional tritium burnup in the plasma. Since SABR burns ~ 15 kg T/year, the minimum inventory was calculated to be ~ 1.6 kg of tritium for a 2-day processing system shutdown. The minimum inventory is a reserve for the processing systems and should be taken into account with the initial condition for startup of the reactor, but ex post facto inclusion of this minimum amount to the initial storage containment condition did not have significant effect on analysis, except for the doubling time because of the larger total inventory. Therefore, the minimum inventory was superimposed with the initial inventory required for startup determined by solving Eq. (5) and calculated to be 2.3 kg.

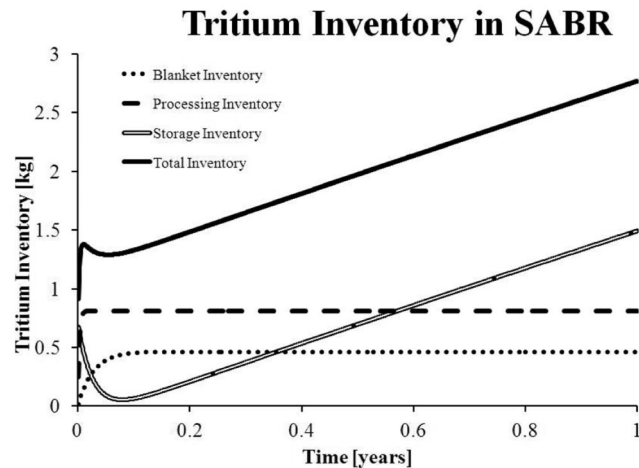


Fig. 14. Tritium inventories in the blanket, processing systems, and storage containment for 1 year after startup.

VI. SHIELDING

Shielding around the plasma and the modular sodium pools, but inside the TF coils, is required to protect sensitive equipment, ensure the SABR design lifetime, and maintain safety barriers. In particular, the SC magnets need to be extensively shielded to limit radiation damage to the SC material and to the electrical insulating material. Because of the geometric complexity and consequent difficulty of replacement, these magnets are designed to last the lifetime of the plant. Thus, the radiation shielding must allow for 40 years of operation at 75% availability, or 30 effective full-power years (FPY) (full power means 500 MW of fusion power plus ~ 3000 MW of fission power), without reaching radiation damage limits on the superconductor or the insulator.

VI.A. Radiation Damage Limits

Radiation damage to the organic insulator in the SC winding pack can cause mechanical failure and is therefore a major concern for limiting the TF magnets' lifetime. Radiation damage to the organic insulators causes elongation, resulting in stresses that will eventually lead to failure of the TF magnets. There is disagreement concerning what values of dose organic insulators can withstand, ranging from 5×10^8 to 10^{10} rads. Originally, glass epoxy was the standard organic insulator; however, as more research comes out, many designs are moving to Kapton and glass-filled polyimides. The SABR design uses the glass-filled polyimide with a generally accepted radiation damage dose limit of $\sim 1 \times 10^9$ rads (Refs. 58 and 59), which is thought to be the lower dose limit of glass-filled polyimide organic insulators.

Radiation damage to the SC material is another concern. The SC magnets must be kept below a critical temperature for superconductivity, and irradiation can cause the critical temperature for superconductivity to decrease in the SC material. The radiation design limit can be specified in terms of neutron fluence, since photon dose seems to have little effect by comparison on the superconductive material. The fast neutron fluence (>0.1 MeV) limit from extensive past studies is set to 1.0×10^{19} n/cm² (Ref. 58).

Another concern is the radiation effects on the copper stabilizer. The copper stabilizer when irradiated undergoes swelling and an increase in electrical resistivity. Calculations on the forced-cooled, cable-in-conduit conductors have shown that stability of the coils can be maintained if the copper stabilizer resistivity (accounting for radiation damage and magnetoresistivity) is ~ 1.2 n Ω ·m or lower.⁵⁸ The initial resistivity for the SABR design is an engineering conservative value of 0.55 n Ω ·m (similar to the initial resistivity value to the conductor used in the MARS design⁶⁰). In addition,

TABLE XIII

Radiation Design Limits*

Radiation Limit	Value
Insulation dosage	1×10^9 rads
Nuclear heating rate	1.0 to 5.0 mW/cm ³
Neutron fluence (>0.1 MeV)	1.0×10^{19} n/cm ²
Copper stabilizer resistivity	1.2 n Ω ·m

*From Refs. 58 and 63.

a design limit of 80% of the stabilizer resistivity limit was used to determine when annealing was necessary. When the resistivity reaches the design limit, annealing at room temperature, which has been found to remove $\sim 80\%$ of the radiation induced resistivity,^{58,60} would be performed.

Although not a radiation damage issue, nuclear heating must be kept within a limit to ensure the cryostat system can keep the SC magnets below their critical temperature. The limit was determined by analyzing the cooling of the field coils under normal and plasma swing conditions with a cryogenic system maximum refrigeration capacity limit of 100 kW at 4 K (Ref. 58). The cryogenic system was divided into four units, each having a capacity of 25 to 30 kW. The design of the SABR cryogenic system for the SC magnets was kept to ITER specifications (Table XIII).

VI.B. Design Process and Modeling

The MCNP5 code⁵⁷ was used to determine the shielding required to meet the design specifications. The MCNP model shown in Fig. 15 and described in Table XIV is a toroidally symmetric (R-Z) approximation of the actual geometry. Therefore, gaps due to discontinuities between the modular sodium pools constituting the annular fission core and the separations between the outer legs of the ten separate TF magnets were not modeled. In addition, to simplify some of the modeling, material homogenization of the fission core, of the coolant through the shielding, divertor case, and of the SC winding pack was performed. For simplicity and a conservative lower shielding thickness, only the divertor structure was considered in homogenizing the divertor region. All calculations were performed with initial BOL material compositions.

The TF magnets are closest to the plasma and fission core and thus likely to receive the highest neutron and photon flux of any of the magnets. Therefore, the shielding is modeled to ensure the lifetime against radiation damage of the TF magnets. If the TF magnets

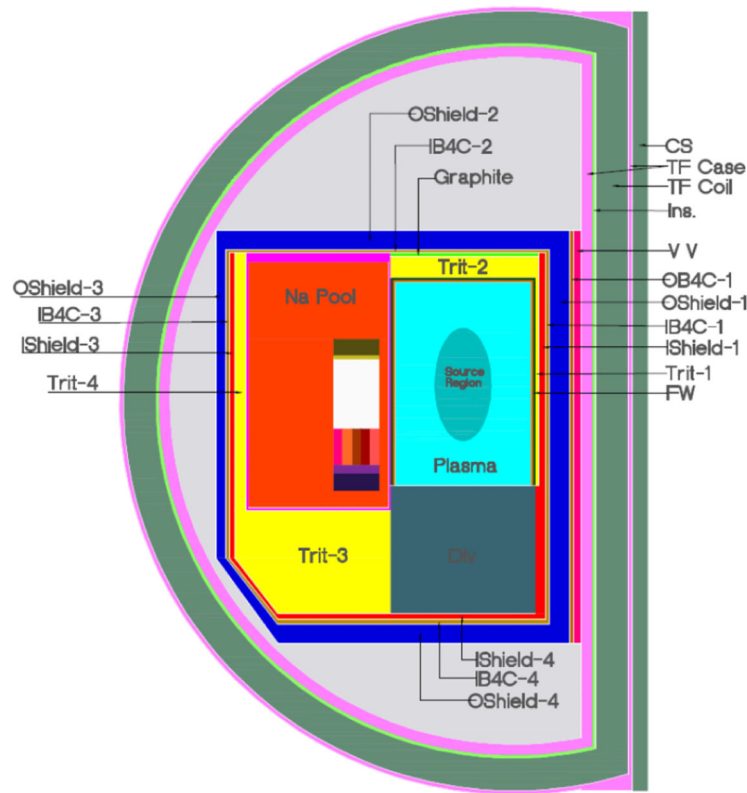


Fig. 15. MCNP model for shielding calculation of SABR.

are sufficiently shielded, it is safe to assume that both the CS and the PF magnets are as well.

Neutrons cause most of the irradiation damage to the copper and SC material; however, the photon dose, especially to the organic insulator, plays a large role as well. Many photons are emitted from the plasma core due to bremsstrahlung, line radiation, and recombination; however, due to their emitted energies and the total shield thickness, these can be considered negligible compared to the photon dose to the SC magnets that accumulate from photons produced from neutron inelastic scattering collisions and radiative capture. There are $\sim 1.8 \times 10^{20}$ D-T reactions per second, each emitting a neutron at 14.1 MeV, when the fusion core is operating at full power (500 MW). The fusion neutrons cause additional neutron sources from fission and $(n,2n)$ reactions that are also accounted for in the calculation.

VI.C. Toroidal Field Coil Representation

Because of the complex geometry of the SC magnets, some assumptions were made to form a homogenous medium to be used for calculations. The TF magnet was split into three regions: a steel case, an effective organic insulator layer, and the toroidal winding pack (housing

the SC and the copper stabilizer). Table XV shows the volumetric percentage of each material that was used for homogenization to make a single TF winding pack region. The maximum dose to the organic insulator is obtained with an effective insulator layer on the inside of the TF magnet winding pack (closest to the plasma). Similar methodology for determining the dose to the organic insulator model is discussed in Refs. 64 through 68.

The TF magnets will use the glass-filled polyimide for the organic insulator to ensure that the TF coils will be able to meet the radiation dose limit. The glass-filled polyimide design has $\sim 5\%$ to 10% more radiation resistant properties than the glass-filled epoxy.^{61,65-68}

VI.D. Shielding Results

The radiation design limits that determined the overall shield thickness were the organic insulator dose, the copper resistivity limit, and the fast neutron fluence limit to the superconductor. The nuclear heating rate condition discussed above appears to be satisfied for all configurations that satisfied the organic insulator dose, the copper resistivity, and the fast neutron fluence limits over the 30-FPY design objective for SABR. As shown in Table XVI, the present shield design protects the TF coils against

TABLE XIV
Shielding Material Descriptions

Name (See Fig. 15)	Materials	Thickness (cm)
TF (toroidal field magnet)	See Table XV	58.12
Ins. (organic insulator)	Effective layer of glass-filled polyimide	4.42
TF case	SS316LN-IG (stainless steel)	
	Outer side	7.08
	Inner side (next to plasma)	20.48
VV	50 vol % ODS steel, 50 vol % He	14.35
Graphite	Graphite with 10 vol % Na	7
FW (first wall) part 1	Beryllium	1
FW part 2	Mix of ODS steel, Na, and CuCrZr	2.2
FW part 3	80 vol % ODS steel, 20 vol % Na	4.9
OB4C	B ₄ C with 5 vol % Na	6.35
OShield-1	WC with 5 vol % Na	36
OShield-2	WC with 5 vol % Na	32.4
OShield-3	WC with 5 vol % Na	18
OShield-4	WC with 5 vol % Na	33
IB4C-1	B ₄ C with 10 vol % Na	6.5
IB4C-2	B ₄ C with 10 vol % Na	7
IB4C-3	B ₄ C with 10 vol % Na	6
IB4C-4	B ₄ C with 10 vol % Na	10
IShield-1	WC with 10 vol % Na	12
IShield-2	WC with 10 vol % Na	n/a
IShield-3	WC with 10 vol % Na	10
IShield-4	WC with 10 vol % Na	10
Trit-1	Li ₄ SiO ₄	6.7
Trit-2	Li ₄ SiO ₄	31.9
Trit-3	Li ₄ SiO ₄	Occupies the space under the Na pool not used for the divertor replacement ports
Trit-4	Li ₄ SiO ₄	28

TABLE XV
Approximate TF Winding Pack Material Representation

Material	Approximate Volume Percent	Density (g/cm ³)
Nb ₃ Sn (SC, non-Cu)	6.4	3.6 (Ref. 72)
Copper	13.91	8.96
Helium (coolant)	13.1	0.000179
SS316LN-IG (stainless steel)	48.32	7.99
Glass-filled polyimide (insulation)	18.27	1.42

radiation damage to the superconductor and to the insulator for times well beyond the 30-FPY design objective, but the copper stabilizer would exceed the radiation design limit before 30 FPY. However, by warming the TF coils up to room temperature, many of the displacements can be removed (annealed). Figure 16 illustrates that by annealing once, the 30-FPY objective can be reached without the copper resistivity exceeding 80% of the limiting value and by annealing twice, the

copper stabilizer is able to achieve 40 FPY without the copper resistivity exceeding 80% of the radiation design limit. By annealing twice, the copper stabilizer can achieve 40.2 FPY without the copper resistivity exceeding 80% of the radiation damage limit.

The 120 nΩ·m stabilizer resistivity design limit used in the above calculations was initially derived for the MARS conductor design operating at 1.8 K and 10 T. An assumption that was made during the MARS calculation

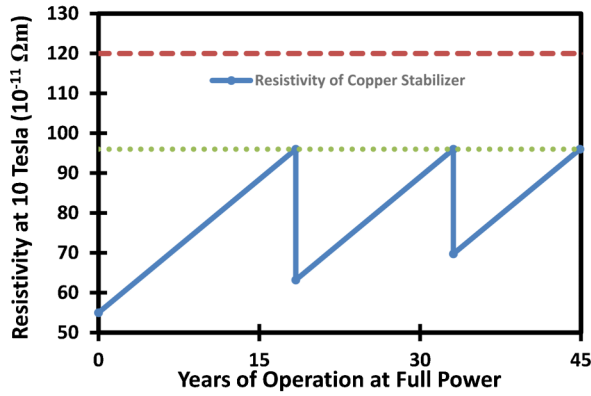


Fig. 16. Copper stabilizer resistivity at 10 T in the TF magnet cable-in-conduit coils of the SABR design as a function of FPY.

was a heat removal transfer limit of 1 W/cm² of area wetted by liquid helium.⁶⁰ This limit could vary somewhat when changing the winding pack design or the cryogenic system. This 120 nΩ·m stabilizer resistivity design limit is considered to be the standard for cable-in-conduit SC coils in general. Additional information on how radiation affects the copper resistivity and the preradiation resistivity values of copper processed by different methods can be found in Ref. 60.

To calculate the copper stabilizer radiation damage, the incoming neutron flux through the TF winding pack was distributed into energy bins. These fluxes were then multiplied by copper resistivity damage rates for each neutron group, to give the average additional copper resistivity per year.⁶⁰ The minimum FPY time until the first annealing cycle is required was calculated using 80% of the resistivity design limit and an initial resistivity of 0.55 nΩ·m to receive ~16.5 years (Ref. 60). The times after the subsequent anneal that a second and then third anneal would be required are ~13.2 and 10.5 years, respectively, as indicated in Fig. 16.

It should be noted that these calculations were made for the maximum 500 MW of fusion power and that SABR would be expected to operate at fusion powers of

200 to 500 MW, so that the actual FPY before reaching the design limit on fast neutron fluence and gamma doses could be 50% to 100% greater than those shown in Table XVI. In any case, we have confidence that the SC magnets would survive against radiation damage for the 30-FPY design lifetime.

The nuclear heating rate is found assuming that all energy deposition from neutrons and photons in the TF magnet is converted to heat. The maximum rate of nuclear heating was determined to be ~0.064 mW/cm³, which is well below the design limit. Additional heat from neutron activated isotopes will result in a slightly larger than predicted nuclear heating rate. Some of the isotopes that could result in additional heating are ¹⁶N, ⁶²Cu, ⁶⁴Cu, ⁵⁶Mn, and more.^{61,62} Activation will not greatly affect the nuclear heating because the neutron flux in the TF magnet is very small, and the magnet materials were chosen to minimize the activation.^{62,69} Additional information supporting the activation data and calculations can be found in Refs. 70 and 71; Ref. 72 provides further information on flux jump limitations to radiation in magnets.

VII. SUMMARY

The SABR is a 3000-MW(thermal) modular sodium pool fast reactor of the IFR/PRISM type fueled by metallic TRU fuel processed from discharged LWR fuel. The neutron source is a D-T fusion tokamak based on ITER physics and technology. Several issues related to the integration of fission and fusion technologies have been addressed in an upgraded conceptual design of SABR. The status of the physics and technology base for SABR is such that it would be technologically feasible to carry out the additional supporting research and development and deploy a first SABR within 25 years.

Refueling a sodium pool fast reactor located within the magnetic coil configuration of a tokamak is a major engineering challenge. We propose a design concept in which the annular fast reactor consists of ten 300-MW(thermal) modular Na pools, each containing 80 fuel assemblies configured in four layers (or rows) radially to

TABLE XVI

Minimum FPY Until Radiation Design Limit Is Met for Any Location on the TF Coil Section

TF Section	FPY Limited by Fast Neutron Fluence	FPY Limited by Insulator Dose	FPY Limited by Stability Resistance for Cryostability (wt% Anneal)
Inside	107.8	61.6	26.1
Top	97.5	39.1	26.3
Outside	1 × 10 ⁶	1 × 10 ⁶	3 × 10 ⁴
Bottom	143.7	56.8	35.6

accommodate up to a four-batch fuel cycle, and an IHX. An entire Na pool module would be disconnected from the secondary heat removal system and removed radially through a refueling port centered at the plasma midplane with dimensions 4.4 m in the vertical direction between adjacent poloidal ring coils and >4.4 m in the toroidal direction between adjacent TF coils. The removed module would be loaded into a transport cask and relocated to a hot cell for refueling and subsequent reloading into SABR. Other Na pool modules would be disconnected from the secondary heat removal system, rotated toroidally to the position of the refueling port, and similarly removed to the hot cell for refueling and subsequent reloading. During operation, the refueling port would be filled with a shielding plug, which would be removed for refueling.

Achieving the reliable long-burn (quasi-steady-state) plasma operation necessary to meet the 75% availability design objective is a major physics challenge that is being vigorously addressed in the worldwide tokamak research program. The SABR design is based on plasma stability, confinement, and other performance parameters in the upper range of those that are routinely achieved today and that will be further demonstrated in the operation of ITER in the 2020s. The long-burn plasma operation will be accomplished with noninductive drive of 4.5 MA of plasma current plus “bootstrap” self-drive of 5.5 MA of plasma current by pressure gradients within the plasma. Electromagnetic wave H&CD power will be used for this purpose (70-MW EC frequency power at 170 GHz and 40-MW LH frequency power at 5 GHz). Access for this electromagnetic H&CD power to the toroidal plasma surrounded by a modular sodium pool fast reactor annulus is a substantial engineering challenge that was addressed by inserting small (~ 1 m toroidally) H&CD access ports between the modular Na pools at two locations separated by 180 deg toroidally. The location of these H&CD access ports adjacent to opposite TF coils allows the rotation of Na pool modules for refueling discussed above.

The ITER SC magnet system was used for the SABR design with only minor modification. The solenoidal magnet core was reduced because the inductive flux requirement for SABR is less than for ITER, and the number of TF coils was reduced from 18 to 10 (which required $\approx 10\%$ increase in coil current to obtain the same 11.8 T field at the conductor as in ITER).

The ITER first-wall and divertor systems were scaled down for the smaller SABR plasma and converted to Na coolant, using the same cooling channels. Suppression of MHD effects on the flow of a liquid metal coolant in a magnetic field was accomplished by lining coolant tubes with SiC to eliminate any current paths into metal structures. A similar technique was employed to prevent current flows in fuel pins, fuel assembly walls, etc.

Tritium breeding Li_4SiO_4 blankets are located inboard of and above the plasma, below the fast reactor,

outboard of the Na pool, and in wedge-shaped modules between the modular sodium pools in the fission annulus. This configuration resulted in a BOL TBR = 1.12. Dynamic tritium inventory calculations based on this BOL configuration suggest that SABR would be tritium self-sufficient, even allowing for downtime for refueling and estimated tritium losses, and could even produce additional tritium to start up subsequent SABRs.

Radiation shielding calculations at a constant 500-MW fusion power indicate that the SC magnets could achieve the lifetime design objective of 40 FPY at 75% availability, with one annealing of the copper resistivity increase. Since the actual fusion power will vary from ~ 200 to 500 MW (and the high-energy fusion neutrons are primarily responsible for the damage), these results indicate that the SC magnets probably would achieve the design lifetime of SABR without annealing.

The purpose of this upgraded conceptual design of SABR is to provide a realistic basis for fuel cycle optimization analyses, dynamic safety analyses to assure the passive safety of both the fission core and the fusion neutron source, and other performance analyses that will contribute to assessing the deployment of a SABR to help close the back end of the nuclear fuel cycle. We plan to carry out such analyses in the near future and hope that others will do likewise.

ACKNOWLEDGMENTS

The work reported in this paper was performed by students in a graduate design course in the Nuclear & Radiological Engineering Program at Georgia Tech under the guidance of professors W.M.S. and A.S.E. The input and advice of many professionals in the field is gratefully acknowledged, in particular, E. A. Hoffman of ANL, whose comments guided the fuel assembly design process; M. A. Abdou of University of California, Los Angeles, whose comments guided the selection of SiC for electrical insulation of metal structures; and B. E. Nelson of Oak Ridge National Laboratory, who guided us to current information on the ITER design. One of the authors (C.L.S.) gratefully acknowledges the support of the U.S. Department of Energy Office of Nuclear Energy’s Nuclear Energy University Programs.

REFERENCES

1. B. R. LEONARD, JR., “A Review of Fusion-Fission (Hybrid) Concepts,” *Nucl. Technol.*, **20**, 161 (1973); <http://dx.doi.org/10.13182/NT73-1>.
2. L. M. LIDSKY, “Fusion-Fission Systems: Hybrid, Symbiotic and Aqueous,” *Nucl. Fusion*, **15**, 151 (1975); <http://dx.doi.org/10.1088/0029-5515/15/1/016>.
3. A. A. HARMS, “Hierarchical Systematic of Fusion-Fission Energy Systems,” *Nucl. Fusion*, **15**, 939 (1975); <http://dx.doi.org/10.1088/0029-5515/15/5/023>.

4. H. A. BETHE, "The Fusion Hybrid," *Nucl. News*, **21**, 7, 41 (May 1978).
5. R. W. MOIR, "The Fusion Breeder," *J. Fusion Energy*, **2**, 351 (1982); <http://dx.doi.org/10.1007/BF01063686>.
6. R. W. MOIR et al., "Fusion Breeder Reactor Design Studies," *Nucl. Technol./Fusion*, **4**, 4, part 2, p. 589 (1983).
7. W. M. STACEY et al., "A TRU-Zr Metal Fuel Sodium Cooled Fast Subcritical Advanced Burner Reactor," *Nucl. Technol.*, **162**, 53 (2008); <http://dx.doi.org/10.13182/NT08-1>.
8. W. M. STACEY, "Georgia Tech Studies of Sub-Critical Advanced Burner Reactors with a D-T Fusion Tokamak Neutron Source for the Transmutation of Spent Nuclear Fuel," *J. Fusion Energy*, **38**, 328 (2009); <http://dx.doi.org/10.1007/s10894-009-9195-0>.
9. M. KOTSCHENREUTHER et al., "Fusion-Fission Transmutation Schemes—Efficient Destruction of Nuclear Waste," *Fusion Eng. Des.*, **84**, 83 (2009); <http://dx.doi.org/10.1016/j.fusengdes.2008.11.019>.
10. W. M. STACEY, "Principles and Rationale of the Fusion-Fission Hybrid Burner Reactor," *AIP Conf. Proc.*, **1442**, 31 (2012).
11. R. W. MOIR et al., "Axisymmetric Magnetic Mirror Fusion-Fission Hybrid," LLNL-TR-484071, Lawrence Livermore National Laboratory (2011).
12. C. L. STEWART and W. M. STACEY, "The SABrR Concept for a Fission-Fusion Hybrid ^{238}U -to- ^{239}Pu Fissile Production Reactor," *Nucl. Technol.*, **187**, 1 (2014); <http://dx.doi.org/10.13182/NT13-102>.
13. C. E. TILL, Y. I. CHANG, and W. H. HANNUM, "The Integral Fast Reactor—An Overview," *Prog. Nucl. Energy*, **31**, 3 (1997); [http://dx.doi.org/10.1016/0149-1970\(96\)00001-7](http://dx.doi.org/10.1016/0149-1970(96)00001-7).
14. Y. I. CHANG et al., "Advanced Burner Test Reactor Preconceptual Design Report," ANL-ABR-1, Argonne National Laboratory (2008).
15. E. A. HOFFMAN, W. S. YANG, and R. N. HILL, "Preliminary Core Design Studies for the Advanced Burner Reactor over a Wide Range of Conversion Ratios," ANL-AFCI-177, Argonne National Laboratory (2008).
16. A. E. DUBBERLEY et al., "Super-PRISM Oxide and Metal Fuel Core Designs," *Proc. 8th Int. Conf. Nuclear Engineering (ICONE 8)*, Baltimore, Maryland, April 2–6, 2000.
17. M. SHIMADA et al., "Chapter 1: Overview and Summary," *Nucl. Fusion*, **47**, S1 (2007); <http://dx.doi.org/10.1088/0029-5515/47/6/S01>.
18. ITER Web Site: www.iter.org.
19. T. S. SUMNER, W. M. STACEY, and S. M. GHIAASIAAN, "Dynamic Safety Analysis of the SABR Subcritical Transmutation Reactor Concept," *Nucl. Technol.*, **171**, 123 (2010); <http://dx.doi.org/10.13182/NT10-4>.
20. C. M. SOMMER, W. M. STACEY, and B. PETROVIC, "Fuel Cycle Analysis of the SABR Subcritical Transmutation Reactor Concept," *Nucl. Technol.*, **172**, 48 (2010); <http://dx.doi.org/10.13182/NT10-3>.
21. C. M. SOMMER et al., "Transmutation Fuel Cycle Analyses of the SABR Fission-Fusion Hybrid Burner Reactor for Transuranic and Minor Actinide Fuels," *Nucl. Technol.*, **182**, 274 (2013); <http://dx.doi.org/10.13182/NT11-55>.
22. V. ROMANELLI et al., "Comparison of the Waste Transmutation Potential of Different Innovative Dedicated Systems and Impact on the Fuel Cycle," *Proc. Int. Conf. Engineering Nuclear Energy Systems (ICENES)*, San Francisco, California, May 15–19, 2011.
23. M. ABDU, "Introduction to MHD and Applications to Thermofluids of Fusion Blankets," Lecture, Institute for Plasma Research, Gandhinagar, India (2007); <http://www.fusion.ucla.edu/abdou/Presentation%20Web%20Page.html#2007>.
24. M. ABDU, University of California, Los Angeles, Personal Communication (2013).
25. M. L. HAMILTON, et al., "Fabrication Technological Development of the Oxide Dispersion Strengthened Alloy MA957 for Fast Reactor Applications," Pacific Northwest National Laboratory (Feb. 2000).
26. D. T. HOELZER et al., "Creep Behavior of MA957 and 14YWT (SM10 heat)," Oak Ridge National Laboratory; http://web.ornl.gov/sci/physical_sciences_directorate/mst/fusionreactor/pdf/Vol.48/3.2_p50-59_Hoelzer.pdf.
27. B. WILSHIRE and T. D. LIEU, "Deformation and Damage Processes During Creep of Incoloy MA957," *Mater. Sci. Eng. A*, **386**, 81 (2004); <http://dx.doi.org/10.1016/j.msea.2004.07.047>.
28. G. RIMPAULT et al., "The ERANOS Code and Data-System for Fast Reactor Analyses," *Proc. Int. Conf. New Frontiers of Nuclear Technology: Reactor Physics, Safety and High-Performance Computing (PHYSOR)*, Seoul, Korea, October 7–10, 2002, American Nuclear Society (2002).
29. C. BOARDMAN, "GE Advanced Liquid Metal Reactor S-PRISM," *Proc. Advisory Committee on Nuclear Safeguards Workshop*, Rockville, Maryland, June 4–5, 2001, U.S. Nuclear Regulatory Commission (2001).
30. "RELAP5-3D Home Page": <http://www.inl.gov/relap5/>, Idaho National Laboratory (Feb. 2013).
31. N. TODREAS and M. KAZIMI, *Nuclear Systems, Volume 2*, p. 77, Hemisphere Publishing Corporation (1990).
32. W. M. STACEY, *Fusion Plasma Physics*, Wiley-VCH Verlag, Berlin, Germany (2005).
33. J.-P. FLOYD et al., "Tokamak Fusion Neutron Source for a Fast Transmutation Reactor," *Fusion Sci. Technol.*, **52**, 727 (2007); <http://dx.doi.org/10.13182/FST07-1>.
34. C. GORMEZANO et al., "Chapter 6: Steady State Operation," *Nucl. Fusion*, **47**, S285 (2007); <http://dx.doi.org/10.1088/0029-5515/47/6/S06>.
35. F. NAJMABADI et al., "The ARIES-AT Advanced Tokamak, Advanced Technology Fusion Power Plant," *Fusion Eng. Des.*, **80**, 3 (2006); <http://dx.doi.org/10.1016/j.fusengdes.2005.11.003>.

36. V. S. CHAN et al., "Physics Basis of Fusion Development Facility Utilizing the Tokamak Approach," *Fusion Sci. Technol.*, **57**, 66 (2010); <http://dx.doi.org/10.13182/FST10-1>.
37. J. DECKER et al., "Calculations of Lower Hybrid Current Drive in ITER," *Nucl. Fusion*, **51**, 073025 (2011); <http://dx.doi.org/10.1088/0029-5515/51/7/073025>.
38. E. POLI et al., "Electron-Cyclotron-Current-Drive Efficiency in DEMO Plasmas," *Nucl. Fusion*, **53**, 013011 (2013); <http://dx.doi.org/10.1088/0029-5515/53/1/013011>.
39. G. L. JACKSON et al., "Noninductive Plasma Initiation and Startup in the DIII-D Tokamak," *Nucl. Fusion*, **51**, 083015 (2011); <http://dx.doi.org/10.1088/0029-5515/51/8/083015>.
40. ITER Technical Basis, Sec. 2.5, "Additional Heating and Current Drive," International Atomic Energy Agency (2001).
41. R. J. LA HAYE et al., "Cross-Machine Benchmarking for ITER of Neoclassical Tearing Mode Stabilization by Electron Cyclotron Current Drive," *Nucl. Fusion*, **46**, 451 (2006); <http://dx.doi.org/10.1088/0029-5515/46/4/006>.
42. F. IMBEAUX et al., "Current Ramps in Tokamaks: From Present Experiments to ITER Scenarios," *Nucl. Fusion*, **51**, 083026 (2011); <http://dx.doi.org/10.1088/0029-5515/51/8/083026>.
43. S. H. KIM et al., "Lower Hybrid Assisted Plasma Current Ramp-Up in ITER," *Plasma Phys. Controlled Fusion*, **51**, 065020 (2009); <http://dx.doi.org/10.1088/0741-3335/51/6/065020>.
44. G. M. D. HOGWEIJ et al., "Optimizing the Current Ramp-Up Phase for the Hybrid ITER Scenario," *Nucl. Fusion*, **53**, 013008 (2013); <http://dx.doi.org/10.1088/0029-5515/53/1/013008>.
45. V. E. LUKASH et al., "Simulation of ITER Plasma Scenarios Starting from Initial Discharge of Central Solenoid," *Proc. 38th Conf. Plasma Physics*, Strasbourg, France, June 27–July 1, 2011, European Physical Society.
46. A. EJIRI et al., "Non-Inductive Plasma Current Start-Up by EC and RF Power in the TST-2 Spherical Tokamak," *Nucl. Fusion*, **49**, 065010 (2009); <http://dx.doi.org/10.1088/0029-5515/49/6/065010>.
47. R. RAMAN et al., "Non-Inductive Plasma Start-Up and Current Ramp-Up in NSTX-U," *Proc. 54th Annual Mtg. APS Division of Plasma Physics*, Providence, Rhode Island, October 29–November 2, 2012, American Physical Society.
48. F. G. RIMINI et al., "Electron Cyclotron Heating and Current Drive Studies During Current Ramp-Up in Tore-Supra," *Plasma Phys. Controlled Fusion*, **47**, 869 (2005); <http://dx.doi.org/10.1088/0741-3335/47/6/009>.
49. ITER Technical Basis, Sec. 2.1, "Magnets," International Atomic Energy Agency (2001).
50. K. TOBITA et al., "Reduction of Energetic Particle Loss by Ferritic Steel Inserts in ITER," *Plasma Phys. Controlled Fusion* **45**, 133 (2003); <http://dx.doi.org/10.1088/0741-3335/45/2/305>.
51. "FLUENT/GAMBIT Version 6.1.22/s.12," *Computational Fluid Dynamics*, Fluent, Inc. (2004).
52. W. M. STACEY, *Fusion*, 2nd ed., Chap. 10, Wiley-VCH, Weinheim (2010).
53. P. ANDREW et al., "Tritium Retention and Clean Up in JET," *Fusion Eng. Des.*, **47**, 233 (1999); [http://dx.doi.org/10.1016/S0920-3796\(99\)00084-8](http://dx.doi.org/10.1016/S0920-3796(99)00084-8).
54. C. H. SKINNER et al., "Studies of Tritiated Co-Deposited Layers in TFTR," *J. Nucl. Mater.*, **290–293**, 486 (2001); [http://dx.doi.org/10.1016/S0022-3115\(00\)00643-7](http://dx.doi.org/10.1016/S0022-3115(00)00643-7).
55. A. A. HAASZ and J. W. DAVIS, "Hydrogen Retention in and Removal from Carbon Materials," *Springer Series in Chemical Physics*, Vol. 78, Springer Publishing Company, Berlin, Germany (2005).
56. M. A. ABDU et al., "Deuterium-Tritium Fuel Self-Sufficiency in Fusion Reactors," *Fusion Technol.*, **9**, 250 (1986).
57. X-5 MONTE CARLO TEAM, "A General Monte Carlo N-Particle Transport Code, Version 5, Volume I, MCNP Overview and Theory," LA-UR-03-1987, Rev. October 3, 2005, Los Alamos National Laboratory (2003).
58. C. HENNING, "Magnet Design Technical Report—ITER Definition Phase," UCID-21681, Lawrence Livermore National Laboratory (1989).
59. "Annex to Design Requirements and Guidelines Level 1 (DRG1): ITER Structural Design Criteria for Magnet Components (SDC-MC)," N 11 FDR 50 01-07-05 R 0.1, ITER.
60. M. W. GUINAN, "Radiation-Effects Limits on Copper in Superconducting Magnets," UCID-19800; CONF-830466-4, Lawrence Livermore National Laboratory (1983).
61. H. Y. ATTAYA, Y. GOHAR, and D. SMITH, "US-ITER Activation Analysis," CONF-901007-49, Argonne National Laboratory (1990).
62. S. J. PIET, "Exploratory Study of Burn Time, Duty Factor, and Fluence on ITER Activation Hazards," EGG-FSP-10396, EG&G Idaho (1992).
63. *Proc. Mtg. Electrical Insulators for Fusion Magnets*, Germantown, Maryland, 1981, U.S. Department of Energy (1981).
64. M. A. SAWAN, "Application of FENDL Nuclear Data to ITER Neutronics and Shielding Analysis," UWFDM-1006, University of Wisconsin (1996).
65. R. R. COLTMAN, JR., C. E. KLABUNDE, and C. J. LONG, "The Effect of a 100 MGy (1010 rads) Gamma-Ray Dose at 5 K on the Strength of Polyimide Insulators," SSD 81-10, Oak Ridge National Laboratory (1981).
66. M. IWATA et al., "Properties of Newly Developed Thermoplastic Polyimide and Its Durability Under Proton, Electron, and UV Irradiations," *Proc. 11th Int. Symp. Materials in a Space Environment*, Aix-en-Provence, France, September 15–18, 2009.
67. N. J. SIMON, "A Review of Irradiation Effects on Organic-Matrix Insulation," NISTIR-3999, National Institute of Standards and Technology (1993).
68. W. MAURER, "Neutron and Gamma Irradiation Effects on Organic Insulating Materials for Fusion Magnets," Kernforschungszentrum Karlsruhe (1985).

69. D. G. CEPRAGA et al., "Neutronics and Activation Calculation for ITER Generic Site Safety Report," *Fusion Eng. Des.*, **63**, 193 (2002); [http://dx.doi.org/10.1016/S0920-3796\(02\)00130-8](http://dx.doi.org/10.1016/S0920-3796(02)00130-8).
70. M. E. SAWAN and H. Y. KHATER, "Initial Nuclear Performance Evaluation of the FIRE Ignition Device," *Proc. 18th Symp. Fusion Engineering*, Albuquerque, New Mexico, October 25–29, 1999, IEEE (1999).
71. M. E. SAWAN and H. Y. KHATER, "Nuclear Analysis of the FIRE Ignition Device," *Fusion Technol.*, **39**, 2, 393 (2001).
72. V. V. KASHIKHIN, "Flux Jumps in Nb₃Sn Magnets," TD-03-005, Fermilab (2003).